Seasonal Variations and Spatial Patterns of Arctic Cloud Changes in Association with Sea Ice Loss during 1950–2019 in ERA5

MATTHEW T. JENKINS,[a] AIGUO DAI,[a] AND CLARA DESER[b]

[a] *University at Albany, State University of New York, Albany, New York*
[b] *National Center for Atmospheric Research, Boulder, Colorado*

(Manuscript received 28 February 2023, in final form 26 October 2023, accepted 31 October 2023)

ABSTRACT: The dynamic and thermodynamic mechanisms that link retreating sea ice to increased Arctic cloud amount and cloud water content are unclear. Using the fifth generation of the ECMWF Reanalysis (ERA5), the long-term changes between years 1950–79 and 1990–2019 in Arctic clouds are estimated along with their relationship to sea ice loss. A comparison of ERA5 to CERES satellite cloud fractions reveals that ERA5 simulates the seasonal cycle, variations, and changes of cloud fraction well over water surfaces during 2001–20. This suggests that ERA5 may reliably represent the cloud response to sea ice loss because melting sea ice exposes more water surfaces in the Arctic. Increases in ERA5 Arctic cloud fraction and water content are largest during October–March from ~950 to 700 hPa over areas with significant (≥15%) sea ice loss. Further, regions with significant sea ice loss experience higher convective available potential energy (~2–2.75 J kg^{-1}), planetary boundary layer height (~120–200 m), and near-surface specific humidity (~0.25–0.40 g kg^{-1}) and a greater reduction of the lower-tropospheric temperature inversion (~3°–4°C) than regions with small (<15%) sea ice loss in autumn and winter. Areas with significant sea ice loss also show strengthened upward motion between 1000 and 700 hPa, enhanced horizontal convergence (divergence) of air, and decreased (increased) relative humidity from 1000 to 950 hPa (950–700 hPa) during the cold season. Analyses of moisture divergence, evaporation minus precipitation, and meridional moisture flux fields suggest that increased local surface water fluxes, rather than atmospheric motions, provide a key source of moisture for increased Arctic clouds over newly exposed water surfaces during October–March.

SIGNIFICANCE STATEMENT: Sea ice loss has been shown to be a primary contributor to Arctic warming. Despite the evidence linking large sea ice retreat to Arctic warming, some studies have suggested that enhanced downwelling longwave radiation associated with increased clouds and water vapor is the primary reason for Arctic amplification. However, it is unclear how sea ice loss is linked to changes in clouds and water vapor in the Arctic. Here, we investigate the relationship between Arctic sea ice loss and changes in clouds using the ERA5 dataset. Improved knowledge of the relationship between Arctic sea ice loss and changes in clouds will help further our understanding of the role of the cloud feedback in Arctic warming.

KEYWORDS: Arctic; Sea ice; Climate change; Cloud cover; Cloud water/phase; Clouds

1. Introduction

Arctic sea ice has been declining over recent decades, accompanied by a lengthening melt season (Stroeve et al. 2014). Loss of sea ice concentration (SIC) increases oceanic absorption of solar radiation in summer and oceanic release of upward longwave (LW) radiation and sensible (SH) and latent (LH) heat fluxes during the cold season due to a steep temperature gradient between the warm ocean surface and frigid overlying air (Royer et al. 1990; Deser et al. 2010; Boeke and Taylor 2018), enhancing Arctic warming (Screen and Simmonds 2010a,b; Serreze and Barry 2011; Boeke and Taylor 2018; Dai et al. 2019). Further, exposed ocean water surfaces are associated with greater cloud fraction and cloud water content than ice-covered surfaces during Arctic autumn (e.g., Kay and Gettelman 2009; Eastman and Warren 2010; Liu et al. 2012; Taylor et al. 2015; Kay et al. 2016; Morrison et al. 2018, 2019). As the Arctic continues to warm and lose sea ice under rising greenhouse gases (GHGs), Arctic cloud amount is projected to increase during the cold season (Vavrus et al. 2009; Philipp et al. 2020). Cloud radiative feedbacks account for a portion of Arctic warming under increased GHGs by enhancing surface downwelling LW radiation (Vavrus 2004; Taylor et al. 2013); however, clouds also cool the Arctic in summer by reflecting shortwave (SW) radiation back to space (Curry et al. 1996; Intrieri et al. 2002b; Alkama et al. 2020; Jenkins and Dai 2021). Changes in Arctic cloud radiative forcing (CRF) impact not only surface temperature but also sea ice extent (Choi et al. 2014; Burt et al. 2016). The complex effects of clouds on the Arctic energy budget and surface warming motivate further investigation into the cloud response to observed sea ice loss.

Clouds play an important role in Arctic top-of-the-atmosphere (TOA) and surface energy balances (Wetherald and Manabe 1988; Intrieri et al. 2002b; Shupe and Intrieri 2004). Jenkins and Dai (2022) showed that clouds contributed ~3 W m^{-2} (−0.25 to −2 W m^{-2}) of TOA forcing during October–March (May–July) from 1950–79 to 1990–2019 based on analyses of the fifth generation of the European Centre for Medium Range Weather Forecasts reanalysis (ERA5). Further, they found that the spatial

Corresponding author: Matthew T. Jenkins, mtjenkins@albany.edu

DOI: 10.1175/JCLI-D-23-0117.1

patterns of Arctic cloud feedback are strongly correlated with sea ice changes in autumn and winter but not in summer. Monroe et al. (2021) found a strong cloud response to wintertime polynyas (i.e., a region with anomalously low SIC). During polynya events, cloud fractions and water contents are larger over the polynya than over surrounding ice-covered regions. Increases in surface downward LW radiation due to enhanced cloudiness over the open water slows refreezing of the sea ice, lengthening polynya events (Monroe et al. 2021). The SW cooling effects of clouds also influence Arctic sea ice extent. Choi et al. (2014) suggest that years with strong cloud cooling and thus reduced surface absorption of solar radiation in spring and early summer increases late summer Arctic sea ice extent. Other studies confirm that springtime cloud warming is associated with low September sea ice extent anomalies (Kapsch et al. 2013; Cox et al. 2016; Huang et al. 2019).

Previous studies have shown a strong (weak) Arctic cloud response to sea ice variations and changes during autumn (summer) using observations (Kay and Gettelman 2009; Palm et al. 2010; Taylor et al. 2015; Morrison et al. 2018), reanalysis products (Schweiger et al. 2008; Cuzzone and Vavrus 2011), and model simulations (Vavrus et al. 2011; Barton and Veron 2012; Morrison et al. 2019). Kay and Gettelman (2009) analyzed the cloud–sea ice relationship during 2006–08 using satellite observations and found that Arctic low cloud fraction was higher over open-water surfaces than ice-covered surfaces in September, but not in summer (i.e., June–August). During the warm summer months, Arctic total cloud fraction depended more on synoptic variability rather than the type of the underlying surface (i.e., ice-covered or open water), while clouds in autumn depended on both the surface types and background atmospheric circulation (Kay and Gettelman 2009). Palm et al. (2010) also found an enhancement of clouds between 0.5 and 2 km over open-water surfaces relative to ice-covered surfaces in early autumn using satellite data during 2003–07. These studies attributed the increased cloud cover to enhanced surface energy and moisture fluxes, a deeper planetary boundary layer, and decreased lower-tropospheric stability over exposed ocean waters. A recent modeling study confirmed that exposed water surfaces enhance low cloud formation in winter (Zheng and Ming 2023).

Schweiger et al. (2008) found a decrease in Arctic low clouds below 800 hPa, but an increase in Arctic midlevel clouds between 800 and 450 hPa during years with anomalously low SIC during 1980–2001 in ERA-40 data. This finding differs from other studies that reported larger increases in low clouds than midlevel clouds over exposed ocean surfaces (Kay and Gettelman 2009; Palm et al. 2010; Morrison et al. 2018, 2019). Schweiger et al. (2008) suggest that large near-surface warming associated with low SIC reduces the lower-tropospheric stability, enhancing vertical mixing and thus midlevel cloud cover. Further, they found that under low SIC conditions, the relative humidity (RH) from 1000 to 950 hPa decreased, diminishing cloud cover near the surface. Model simulations confirm decreased RH between 1000 and 950 hPa, but increased RH above 950 hPa, leading to suppressed (enhanced) cloud fraction below (above) 950 hPa (Abe et al. 2016) in response to Arctic sea ice loss. Thus, there still exist inconsistencies regarding how low and middle clouds may respond to sea ice loss. An improved understanding of the vertical profiles of cloud properties and the dynamic and thermodynamic processes influencing Arctic cloud profiles is needed because cloud height influences CRF and cloud feedback (Zelinka et al. 2012).

The primary goals of this study are to analyze the seasonality, vertical structure, and spatial patterns of Arctic cloud property changes (i.e., in cloud fraction, and cloud liquid and ice water contents) over areas with and without significant sea ice loss from ERA5 data and to improve understanding of the atmospheric conditions that link sea ice loss to enhanced cloud amount. Specifically, we seek to answer the following questions:

1) How is the long-term sea ice loss from 1950 to 2019 related to changes in Arctic clouds at different levels, atmospheric stability, and other related fields in terms of their spatial patterns, seasonality, and physical linkages?
2) What dynamic and thermodynamic processes drive increases in Arctic cloud fraction and/or cloud water content in response to sea ice loss and how do changes in these dynamic and thermodynamic processes vary seasonally?
3) Do increases in Arctic cloud properties over areas with sea ice loss result from enhanced remote moisture transport or increased local evaporation due to sea ice loss?

A better understanding of the local cloud response to Arctic sea ice loss will improve estimates of Arctic cloud feedback, which is a major source of uncertainty in future climate projections (Soden et al. 2004; Gettelman and Sherwood 2016; Ceppi et al. 2017).

In this study, we use the ERA5 dataset (Hersbach et al. 2020) to investigate changes in Arctic cloud properties and atmospheric conditions over areas with and without large sea ice loss between 1950–79 and 1990–2019. Our focus on long-term changes distinguishes our study from early work that analyzed the cloud response to sea ice variations and changes over shorter time periods (e.g., Schweiger et al. 2008; Kay and Gettelman 2009; Morrison et al. 2018). After introducing the data and methods in section 2, we evaluate ERA5 cloud fraction against satellite-based products in section 3. We then document the spatial patterns, vertical profiles, and seasonality of long-term Arctic cloud changes in ERA5 in section 4 and describe the changes in atmospheric conditions over areas with large sea ice loss and explore their physical linkages to Arctic cloud changes in section 5. We summarize and discuss the results in section 6. Our findings suggest new mechanisms and synthesize previous findings that may link sea ice loss to Arctic cloud changes.

2. Data and methods

a. ERA5

As long-term observations over the Arctic Ocean are sparse, we use monthly data from 1950 to 2019 from ERA5 (Hersbach et al. 2020) on a 1.0° latitude–longitude grid. We

analyze three-dimensional fields of cloud fraction, and specific cloud liquid and ice water contents. Further, we examine changes in SIC, surface air temperature, convective available potential energy (CAPE), planetary boundary layer height (PBLH), vertically integrated moisture divergence, total precipitation, surface evaporation, and vertical profiles of air temperature, vertical velocity, horizontal divergence, specific humidity, and relative humidity. We select the 1000, 950, 900, 850, 700, 600, and 500 hPa levels for three-dimensional variables. Graham et al. (2019b) showed that ERA5 outperforms other reanalysis datasets in reproducing vertical profiles of temperature, wind, and specific humidity in the Arctic region. ERA5 SIC incorporates the second version of the Hadley Centre Global Sea Ice and Sea Surface Temperature (HadISSTv2) product for years 1950–78 and the Operational Sea Surface Temperature and Ice Analysis (OSTIA) for 1979 to the present (Hersbach et al. 2020). We use ERA5 SIC fields because satellite-based sea ice observations are not available prior to 1979. Both OSTIA and HadISSTv2 produce similar interannual variability and trends for Arctic SIC, especially over areas that are predominantly ice-covered (i.e., SIC $\geq$ 50%). For areas where SIC $\geq$ 10%, OSTIA Arctic-mean SIC is slightly greater than HadISSTv2 for 1979–2019. We do not expect any discrepancies in ERA5 SIC to affect our conclusions because ERA5 captures the interannual variability, seasonal cycle, and trends in Arctic sea ice well for the postsatellite period (Hirahara et al. 2016).

We focus on the changes in cloud properties and atmospheric conditions between years 1950–79 and 1990–2019. Local air temperatures remained stable during 1950–79, but large Arctic warming occurred from 1990 to 2019 (England et al. 2021). Thus, the 1990–2019 minus 1950–79 difference estimates how recent sea ice loss may have impacted Arctic cloud properties and atmospheric conditions, even though ocean–atmosphere interactions are two-way. ERA5 incorporates observations of surface pressure, temperature, and wind speed from a variety of historical archives (e.g., the International Surface Pressure Databank, the Comprehensive Historical Upper Air Network, etc.) to generate data prior to 1979. We caution that satellite-based observations are not assimilated into ERA5 data prior to 1979; however, confidence in the ERA5 data increases from 1950 to 1978, where the number of observations incorporated into the reanalysis increases from ~53 000 to 570 000 observations per day (Bell et al. 2021). The 1980–89 decade experienced small local warming in the Arctic region relative to years 1990–2019 and is excluded from the analysis. However, a linear trend analysis for years 1980–2020 reveals similar spatial patterns of cloud changes as the long-term difference (not shown). Therefore, we do not expect exclusion of years 1980–89 to qualitatively affect our conclusions.

To assess the impact of sea ice loss on Arctic clouds and atmospheric conditions, we separate the Arctic Ocean into areas with significant ($\geq$15%) or little (<15%) SIC loss (excluding land) between 1950–79 and 1990–2019. Areas with 15% or greater sea ice loss are located mostly along the 1950–79 marginal ice zones, which became mostly open water by 1990–2019. We average and group the data by month for each 30-yr period to examine the mean seasonal cycle and its change for each variable. Huang et al. (2019) showed that the atmosphere and ocean are tightly coupled in March, but the influence of sea ice on the atmosphere weakened April–June. Thus, we define the cold (warm) season as October–March (April–September) to investigate the role of strong (weak) ocean–atmosphere coupling on cloud–sea ice interactions. The Arctic region is mainly ocean surface north of the Arctic Circle; therefore, we define the Arctic as the region poleward of 67°N for area-weighted averages. However, we show the region poleward of 55°N to include the Sea of Okhotsk and Hudson Bay on maps. We estimate the statistical significance of temporal and spatial correlations with a two-tailed Student's t test. For this study, a statistically significant correlation has an associated p value less than 0.01.

ERA5 cloud properties are based on the Tiedtke (1993) cloud scheme, which estimates clouds by resolving processes that are cloud water sources (e.g., condensation, sublimation, or cumulus convection) or sinks (e.g., precipitation or cloud evaporation). Yeo et al. (2022) evaluated Arctic clouds in ERA5 by comparing ERA5 cloud properties to *CloudSat* and *Cloud-Aerosol Lidar and Infrared Pathfinder Satellite Observation* (*CloudSat*/*CALIPSO*) data for July 2006–June 2010. For cloud fraction, ERA5 simulates more clouds over sea ice relative to ocean water surfaces. Further, ERA5 cloud liquid and ice water paths are smaller than satellite observations over the entire Arctic region. Despite these discrepancies, ERA5 produces a reasonable seasonal cycle of Arctic midlevel (i.e., 800–450 hPa) cloud fraction, high (i.e., ≤450 hPa) cloud fraction, liquid water path, and ice water path, suggesting that ERA5 captures the seasonality of Arctic clouds properties well. Further, the differences between *CloudSat*/*CALIPSO* and ERA5 mean low cloud fraction and cloud vertical profiles are reduced over open-water surfaces compared to ice-covered areas (Yeo et al. 2022). Due to the potential biases in ERA5 cloud variables, we compare ERA5 cloud fraction and CRF to data from the Clouds and the Earth's Radiant Energy System (CERES; Wielicki et al. 1996) project.

b. *CERES energy balanced and filled data*

We compare monthly ERA5 cloud fields and CRF data to those from version 4.1 of the CERES energy balanced and filled (EBAF; Loeb et al. 2018) and edition 4A of the CERES synoptic (SYN1deg; Doelling et al. 2016) datasets from January 2001 to December 2020. CERES cloud fields are based on observations from the Moderate Resolution Imaging Spectroradiometer (MODIS) for both daytime and nighttime. MODIS uses passive remote sensing techniques that rely on reflected SW radiation and emitted LW radiation to infer radiative fluxes and cloud properties. For March 2000 to February 2017, MODIS Collection 5 is used in CERES, but for March 2017 to the present, CERES uses MODIS Collection 6 (Kato et al. 2018). In the Arctic region, MODIS underestimates clouds over sea ice (by ~10%–20%) especially at night due to the low contrast in albedo and thermal emissions between clouds and ice-covered surfaces (Liu et al. 2010). *CloudSat*/*CALIPSO* satellite observations (which rely on

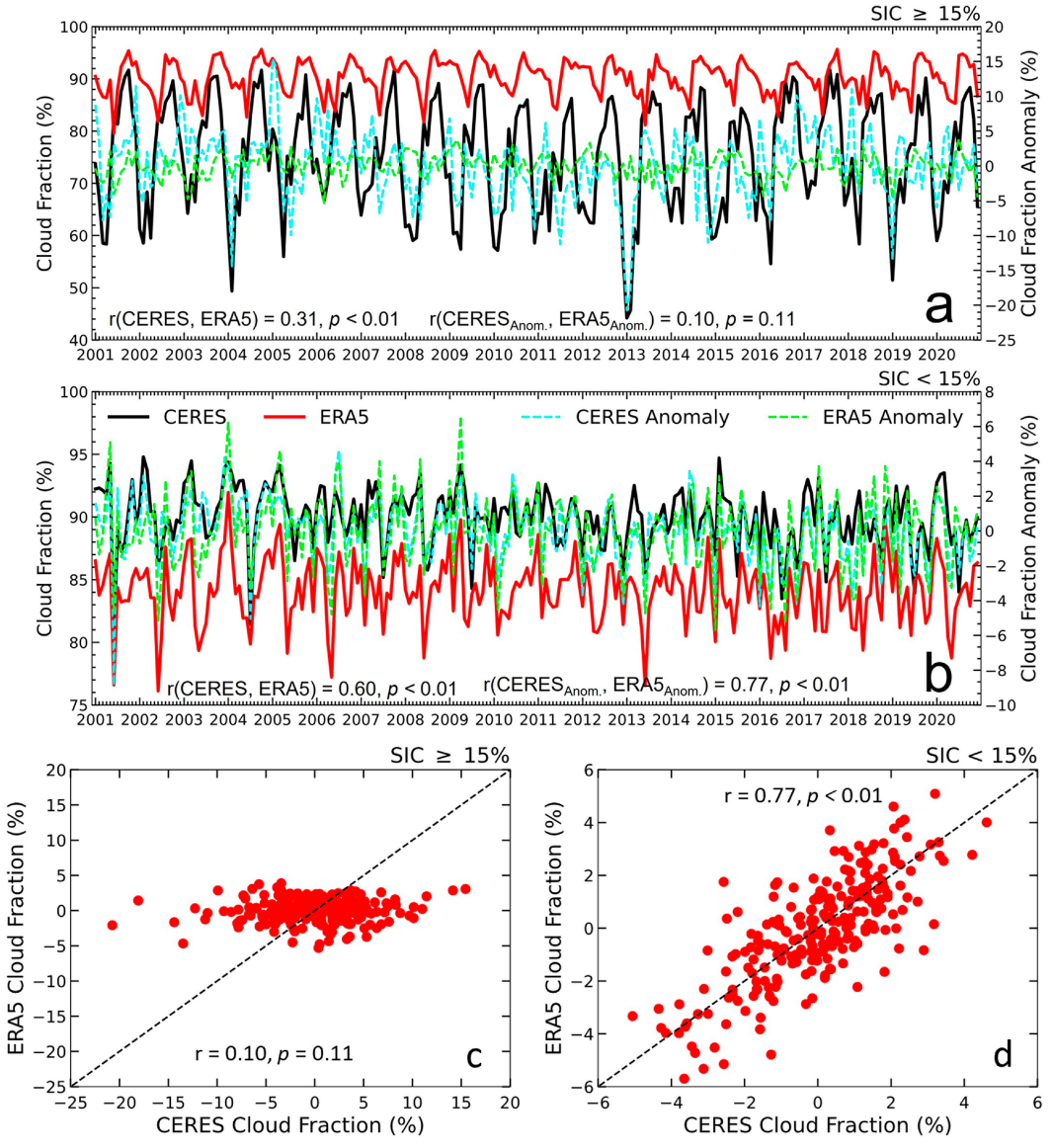

FIG. 1. (a),(b) Time series of monthly cloud fraction (in %) from January 2001 to December 2020 averaged over oceanic areas with 2001–20 annual mean sea ice concentration (a) greater than or equal to 15% or (b) less than 15% for ERA5 (solid red and dashed green lines) and CERES (solid black and dashed cyan lines) data with the seasonal cycle included (left *y* axis; solid lines) and mean seasonal cycle removed (right *y* axis; dashed lines). The correlation coefficient (*r*) and associated *p* value between the time series are shown. (c),(d) ERA5 vs CERES monthly Arctic (67°–90°N) cloud fraction (in %; years 2001–20; mean seasonal cycle removed) averaged over ocean surfaces for areas with (c) mean SIC ≥ 15% or (d) mean SIC < 15%.

active remote sensing) are also commonly used to study Arctic cloud properties (e.g., Taylor et al. 2015; Morrison et al. 2018), but data poleward of 82°N are unavailable (e.g., Liu et al. 2010; Taylor et al. 2015). Further, *CloudSat*/*CALIPSO* may not capture clouds below 1 km well due to surface clutter and/or attenuation of the lidar beam used to retrieve atmospheric conditions (Intrieri et al. 2002a; Zygmuntowska et al. 2012).

We compare total cloud fraction, CRF, and cloud liquid and ice water paths from CERES and ERA5 over their period of overlap (i.e., 2001–20). Combined observations from the *Terra* and *Aqua* satellites are included after July 2002 in CERES, but data only from *Terra* are available prior to this date. To roughly estimate the impact of SIC on cloud fractions and other related fields in ERA5 and CERES, we compute averages over areas where the mean SIC for 2001–20 is less than 15% (excluding land) and over regions where the mean SIC is 15% or more. We also compare the seasonal cycle of the CRF at both the TOA and surface from ERA5 and CERES, where the CRF is defined as the all-sky minus

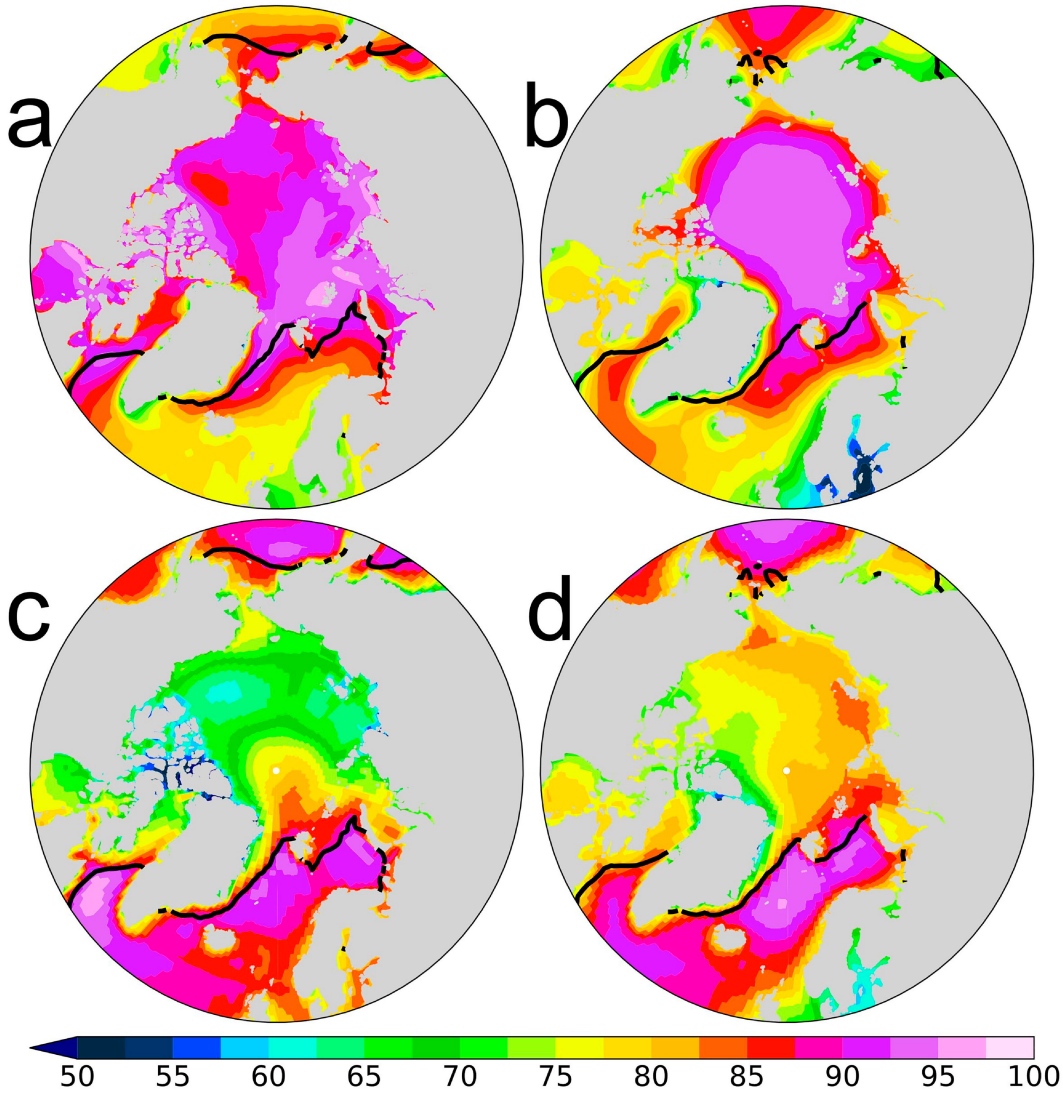

FIG. 2. (a),(b) ERA5 and (c),(d) CERES total cloud fraction averaged over years 2001–20 for (a),(c) October–March and (b),(d) April–September. The black contour represents the mean 15% sea ice concentration based on ERA5 data. The MODIS clouds used in CERES likely underestimate cloud amount by 10%–20% over the polar ice cap, especially during the polar night (Liu et al. 2010).

clear-sky total (i.e., SW + LW) radiative flux difference. We emphasize that section 3 includes only a brief comparison of ERA5 cloud fraction to one satellite-based product, and that other studies (e.g., Yeo et al. 2022) provide a more detailed evaluation of Arctic clouds in reanalysis datasets.

3. Comparison of CERES and ERA5 cloud fraction and CRF

The time series of Arctic-mean monthly cloud fraction from ERA5 and CERES are closely related when averaged over water surfaces ($r = 0.60$, $p < 0.01$; Fig. 1b), but are less well correlated when averaged over areas containing sea ice ($r = 0.31$, $p < 0.01$; Fig. 1a). After removing the mean seasonal cycle, which is largest in CERES over sea ice, the correlations change to 0.77 (Figs. 1b,d) and 0.10 (Figs. 1a,c) over Arctic water and ice surfaces, respectively. Cloud fraction over sea ice–covered surfaces tend to be higher in ERA5 (~85%–95%) than CERES (~50%–90%), partly due to the underestimation of cloud fraction over sea ice by MODIS (Liu et al. 2010); however, the seasonal variations are much smaller in ERA5 than CERES over sea ice (Fig. 1a). Over water surfaces, the ERA5 and CERES cloud fractions show comparable amplitudes of variations, with CERES exhibiting slightly greater cloud amount (i.e., ~87% for ERA5 vs ~92% for CERES) (Fig. 1b). We also briefly compare monthly cloud liquid and ice water paths between ERA5 and CERES data for years 2001–20 (not shown). Like cloud fraction, the relationship between ERA5 and CERES cloud liquid and ice water path is weak over ice-covered surfaces and is strongest

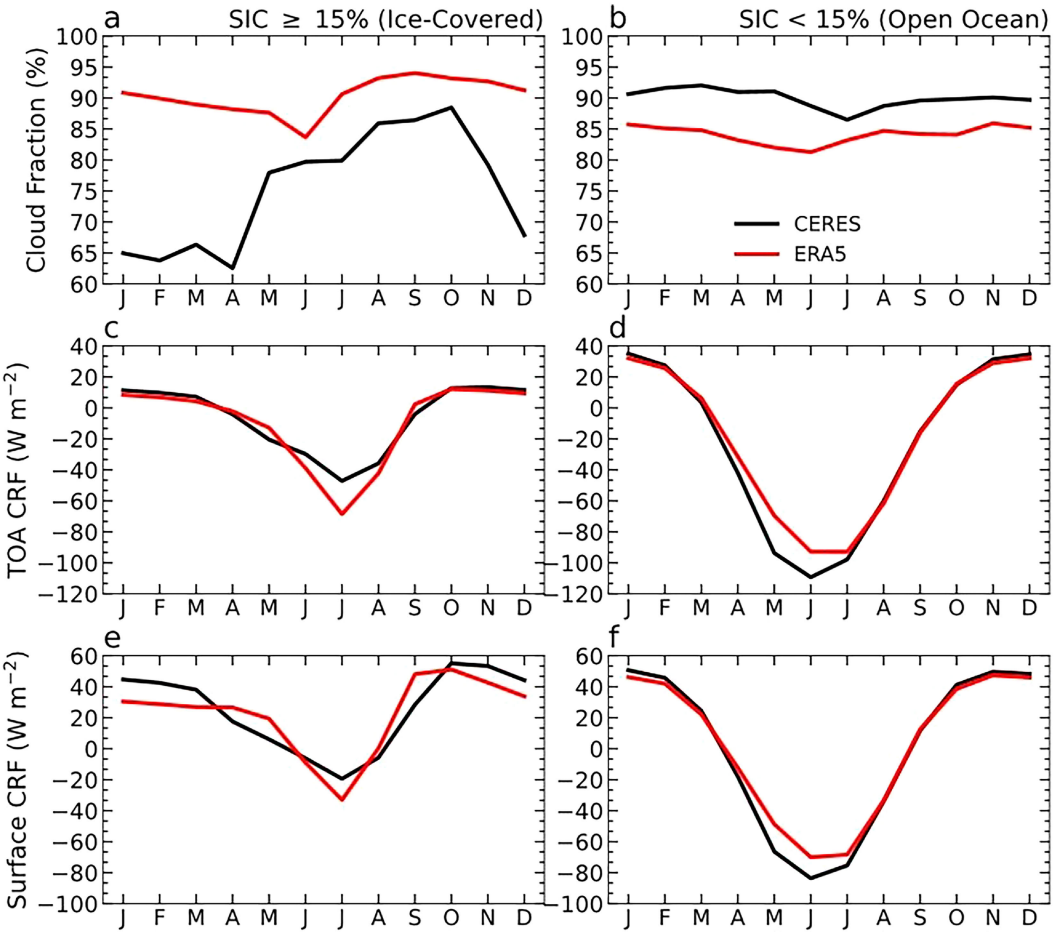

FIG. 3. Seasonal cycle (years 2001–20) of (a),(b) cloud fraction (in %), (c),(d) net TOA cloud radiative effect (in W m^{-2}), and (e),(f) net surface cloud radiative effect (in W m^{-2}) for CERES (black lines) and ERA5 (red lines) data averaged over ocean surfaces with (a),(c),(e) mean sea ice concentration ≥ 15% and (b),(d),(f) mean sea ice concentration < 15%. The MODIS clouds used in CERES significantly underestimate cloud amount over sea ice during the polar night (Liu et al. 2010), which contributes to the low cloud fraction from November–April shown in (a).

over regions with 15% or less sea ice, with correlation coefficients of 0.42 and 0.25, respectively.

Next, we examine the spatial patterns (Fig. 2) and seasonal cycles (Figs. 3a,b) of the 2001–20 mean Arctic cloud fraction in ERA5 and CERES. Spatially, ERA5 mean cloud amounts are ~90%–100% over areas poleward of the 15% mean sea ice edge in each season, higher than open-water ocean surfaces (Figs. 2a,b). In contrast, cloud fraction in CERES is generally lower over sea ice–covered areas than open-water ocean surfaces (Figs. 2c,d), especially during October–March (Fig. 2c). The MODIS clouds used in CERES likely overestimate the water-versus-ice difference due to its underestimation of clouds over sea ice (Liu et al. 2010). High lower-tropospheric stability over ice-covered surfaces contributes to enhanced cloud cover over sea ice relative to open-water ocean surfaces in ERA5 (Yeo et al. 2022). The discrepancy of total cloud fraction over sea ice is also present in the seasonal cycle of cloud fraction, with ERA5 showing a weak minimum in June while CERES shows elevated cloudiness during May–October (Fig. 3a), partly due to its underestimation of cloudiness over sea ice during the polar night in the winter months (Liu et al. 2010). Cloud fraction averaged over open-water ocean surfaces does not vary significantly throughout the year in both CERES and ERA5, with slightly higher cloud fraction in CERES (Fig. 3b). The difficulties in measuring clouds over Arctic sea ice by satellites present a challenge for us to validate ERA5 clouds there.

As stated above, clouds play an important role in the Arctic TOA and surface energy balances. Figures 3c–f show the mean seasonal cycle of the net CRF averaged over regions with 15% or greater mean SIC or regions with less than 15% SIC (excluding land) at the TOA and surface. Despite the differences in mean cloud fraction (Figs. 3a,b), ERA5 and CERES show good agreement for the TOA and surface CRF with negative CRF (of 20–100 W m^{-2}) during April–September (i.e., the sunlit months) and positive CRF (up to 50 W m^{-2}) during October–March (i.e., polar night) (Figs. 3c,f). ERA5 and CERES show a larger negative CRF over open-water surfaces

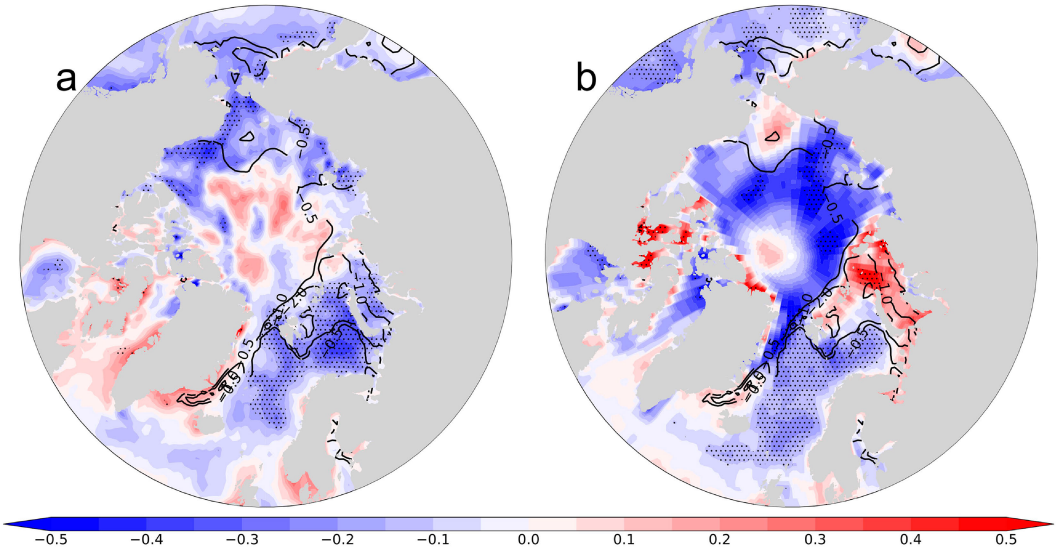

FIG. 4. October–March linear trend maps for (a) ERA5 and (b) CERES total cloud fraction (in % yr^{-1}; shading) and ERA5 sea ice concentration (in % yr^{-1}; contours) for years 2001–20. Statistically significant cloud fraction trends at the 0.05 level are stippled.

(Figs. 3d,f) than ice-covered surfaces (Figs. 3c,e) for both the TOA (Fig. 3d) and surface CRF (Fig. 3f) in June–August due to the larger albedo differences between the water surfaces and clouds. In other words, the cloud albedo effect is more effective over dark water surfaces than over reflective ice surfaces because most sunlight under clear skies would be reflected by sea ice without clouds, but it would be absorbed by dark water surfaces. The TOA CRF is similar in ERA5 and CERES during October–March with a value of ~15 W m^{-2} over the Arctic (Fig. 3d) and ice-covered surfaces (Fig. 3e) and ~20–30 W m^{-2} over ocean water surfaces (Fig. 3f). The cold-season CRF warms the surface by ~30–40 W m^{-2} in CERES and ERA5 over ice-covered surfaces (Fig. 3e), and ~50 W m^{-2} over open-water surfaces (Fig. 3f).

Last, we examine the 2001–20 trend maps of ERA5 (Fig. 4a) and CERES (Fig. 4b) cloud fraction. Statistically significant negative cloud fraction trends occurred in the Norwegian Sea for both ERA5 (Fig. 4a) and CERES (Fig. 4b) during October–March. A discrepancy in the ERA5 and CERES cloud fraction trends occurred over the Barents–Kara and Chukchi Seas, with decreasing clouds in ERA5 and increasing clouds in CERES. Over most of the central Arctic Ocean, cloud fraction trends were statistically insignificant at the 0.05 level in ERA5 and CERES in autumn and winter (Fig. 4). Although there are statistically insignificant, divergent cloud fraction trends in the central Arctic between ERA5 and CERES, we emphasize that this study focuses on long-term cloud changes in relation to sea ice loss, which occurs primarily along the marginal ice zones. Thus, the central Arctic region is not a key focus of this study due to negligible sea ice or cloud field changes there. Further, the short 20-yr record of CERES data or differences in cloud fraction vertical profiles may account for the discrepancies between the 2001–20 ERA5 and CERES total cloud fraction trend maps.

Our comparison of the ERA5 and CERES cloud fraction data shows that ERA5 simulates cloud fraction well over open-water surfaces during 2001–20 (Fig. 1b) but show higher cloud fraction in sea ice–covered regions with reduced seasonal variations than CERES (Fig. 2), consistent with Yeo et al. (2022). The strong agreement between ERA5 and CERES cloud fraction averaged over open-water surfaces suggests that ERA5 may be able to capture the cloud response to sea ice loss because melting sea ice exposes more ocean waters. We emphasize that while Arctic cloud data in ERA5 contain mean biases relative to CERES, the main goals of this paper are to further reveal and understand the processes leading to the enhanced cloud amount over regions with sea ice loss. The underestimation of clouds over sea ice in CERES data does not necessarily suggest that ERA5 overestimates clouds over sea ice–covered areas. As the ice-covered areas mainly include regions around the North Pole where atmospheric conditions (e.g., stability) are quite different from those near the marginal ice zone (where long-term sea ice loss occurs), such opposite differences between ice-covered and open-water surfaces do not necessarily reflect the cloud response to sea ice loss along the marginal ice zone, which is the focus of our subsequent analysis. The lack of ground-based in situ observations and the limitations of remote sensing techniques make evaluation of ERA5 clouds challenging in the Arctic.

4. Climatology and long-term changes in ERA5 cloud properties

We examine the 1950–79 climatology and long-term changes (i.e., years 1990–2019 minus years 1950–79) in ERA5 cloud fraction, and specific cloud liquid and ice water contents for regions that experienced significant (≥15%) or little (<15%) sea ice loss. Figure 5a shows that from 1950–79 to 1990–2019, ERA5

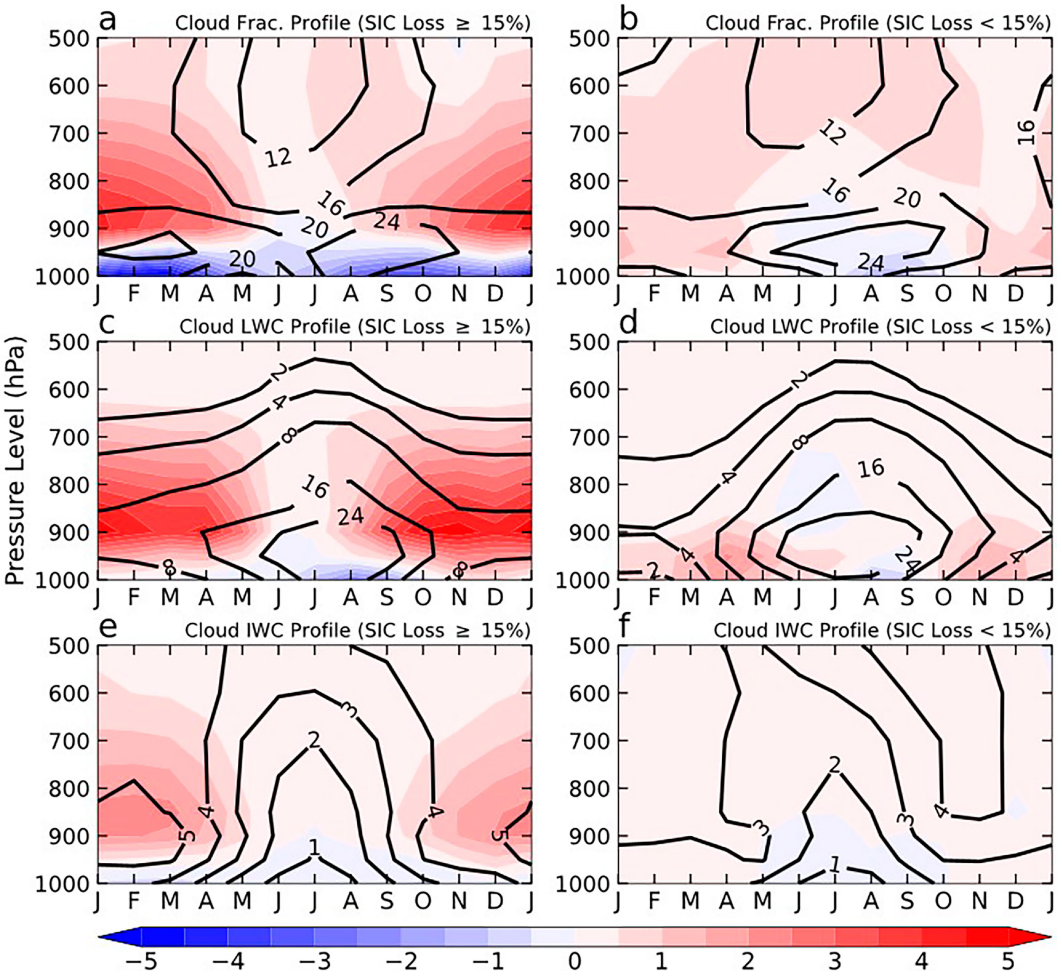

FIG. 5. Arctic (67°–90°N) monthly mean climatology for years 1950–79 (contours) and long-term changes (years 1990–2019 minus 1950–79; shading) as a function of months and pressure levels in ERA5 (a),(b) cloud fraction (in %), (c),(d) specific cloud liquid water content (LWC; in mg kg^{-1}), and (e),(f) specific cloud ice water content (IWC; in mg kg^{-1}) averaged over the oceanic areas (a),(c),(e) with 15% or greater SIC loss and (b),(d),(f) with less than 15% SIC loss.

cloud fraction increased by ~5%–6% around 950–700 hPa but decreased by similar amounts near the surface (1000–950 hPa) during October–March over regions with significant sea ice loss (mainly around the marginal ice zones; Fig. 6d). Changes in Arctic cloud amount were small from May to August throughout the entire vertical profile (Figs. 5a,b), or above 700 hPa (Fig. 5a) and over oceanic regions with little sea ice loss (Fig. 5b) throughout the year. The oceanic regions with little sea ice loss include both open-water surfaces and ice-covered areas well below the ice melting temperature (Fig. 6d). We notice that areas with little sea ice loss experienced slight increases in cloud fraction over the central Arctic (i.e., ~1%–3%) and decreases in cloud fraction in the Norwegian and Barents Sea areas during October–March (Fig. 6d). To examine the effects of the large decrease in North Atlantic clouds on Arctic mean cloud changes, we average Arctic cloud properties over 55°–70°N to exclude the central Arctic region, which is mostly ice-covered through the winter season (Fig. 2a). We found that our results in Figs. 6a–c are not qualitatively impacted by excluding the central Arctic from the domain (not shown).

Mean cloud liquid water content (LWC) was largest from May to August near 950 hPa over both areas with and without large sea ice loss and was smaller during October–March (Figs. 5c,d). In contrast, the mean cloud ice water content (IWC) was largest from December to March, especially over areas with significant sea ice loss (Fig. 5e), but was negligible in summer, likely due to seasonal changes in air temperature and phase of cloud droplets. Over areas with significant sea ice loss, cloud LWC increased by ~3–7 × 10^{-3} g kg^{-1} (~37.5% of the 1950–79 mean; Fig. 5c) and cloud IWC increased by ~1–3 × 10^{-3} g kg^{-1} (~26.7%; Fig. 5e) around 950–700 hPa during October–March. Thus, cloud LWC increased more than cloud IWC in absolute and relative values in autumn and winter from 1950–79 to 1990–2019. Changes in cloud LWC (Fig. 5d) and IWC (Fig. 5f) were negligible during summer, over areas with little sea ice loss, and near the surface.

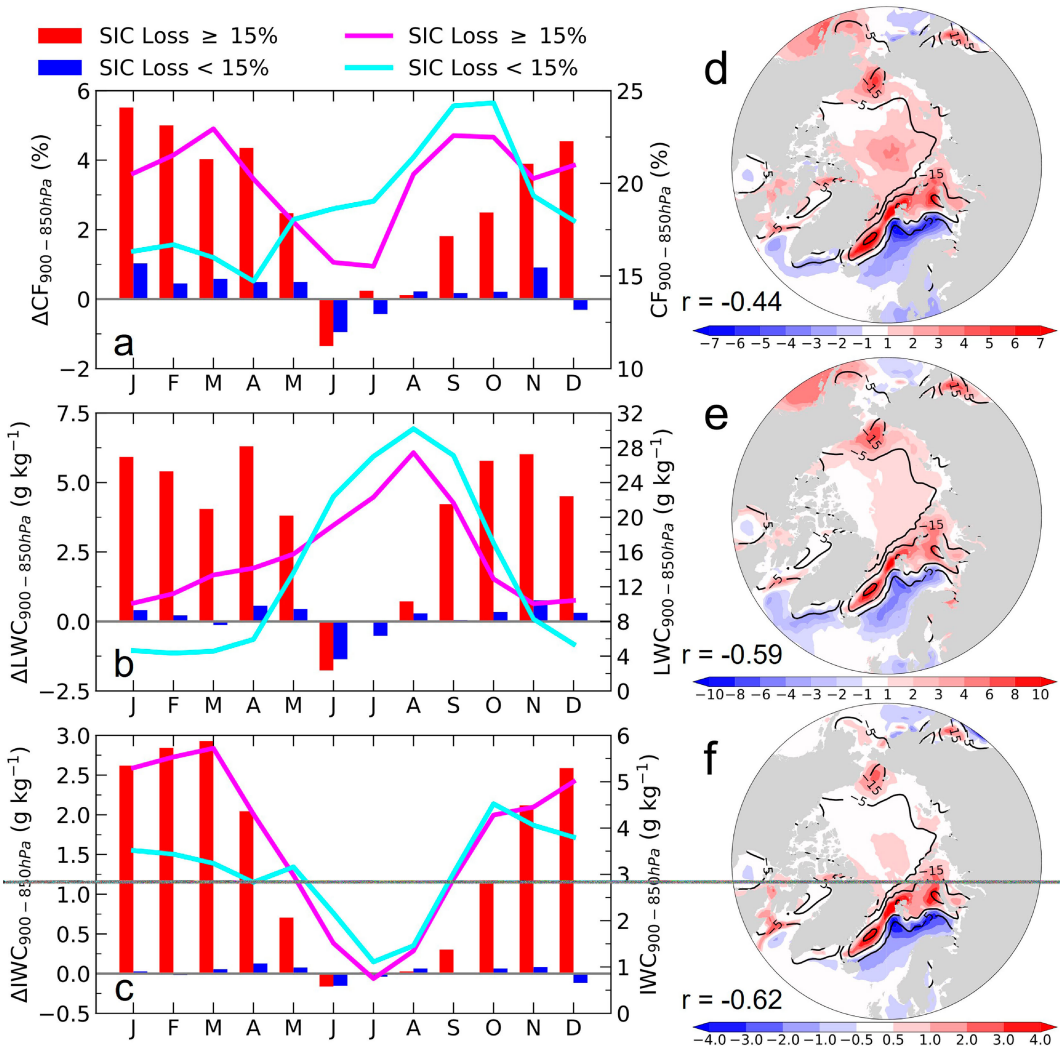

FIG. 6. (a)–(c) Long-term changes (bars; left *y* axis; years 1990–2019 minus years 1950–79) in ERA5 (a) cloud fraction (in %), (b) cloud liquid water content (in mg kg^{-1}), and (c) cloud ice water content (mg kg^{-1}) for 900–850 hPa averaged over areas with 15% or greater SIC loss (red bars) and areas with less than 15% SIC loss (blue bars) poleward of 67°N. The corresponding 1950–79 mean seasonal cycle for each variable averaged over areas with SIC loss ≥ 15% (pink line), and areas with SIC loss < 15% (cyan line) is shown on the right *y* axis. (d)–(f) Long-term changes in ERA5 October–March sea ice concentration [shown as contours in (d)–(f), with contour levels at −5, −15, and −30], (d) cloud fraction (shading; in %), (e) cloud liquid water content (shading; in mg kg^{-1}), and (f) cloud ice water content (shading; in mg kg^{-1}) for 900–850 hPa. The corresponding pattern correlation between the shaded and contour field is shown in the bottom-left corner of (d)–(f). Each correlation coefficient has a *p* value less than 0.01. For (a)–(c), changing the averaging domain to 55°–70°N to exclude the polar ice cap, which is a major part of the area with <15% SIC loss, does not alter the results qualitatively.

Changes in Arctic cloud fraction (Fig. 6a), LWC (Fig. 6b), and IWC (Fig. 6c) averaged over 900–850 hPa were greatly enhanced over areas with significant sea ice loss compared to regions with little sea ice loss during October–April. Specifically, the October–April Arctic cloud fraction, LWC, and IWC increased by ~4%–6% of the sky, ~5.0–7.5 × 10^{-3} g kg^{-1} (~46.2% of the 1950–79 mean), and ~2–3 × 10^{-3} g kg^{-1} (~47.1% of the 1950–79 mean), respectively, over areas with significant sea ice loss. Note that the 1950–79 mean cloud LWC (Fig. 6b) and IWC (Fig. 6c) showed a similar seasonal cycle over areas with and without significant sea ice loss, with cloud LWC peaking in summer and IWC peaking in winter. The 1950–79 climatology of the cloud fraction averaged over 900–850 hPa showed surface dependence mainly during January–April, with a maximum cloud fraction (~20%–25%) during October–March over areas with significant sea ice loss and peak cloud fractions (~25%) in September and October in regions with little sea ice loss (Fig. 6a). Spatially, the long-term changes in October–March cloud fraction (Fig. 5d), cloud LWC (Fig. 6e), and IWC (Fig. 6f) are moderately

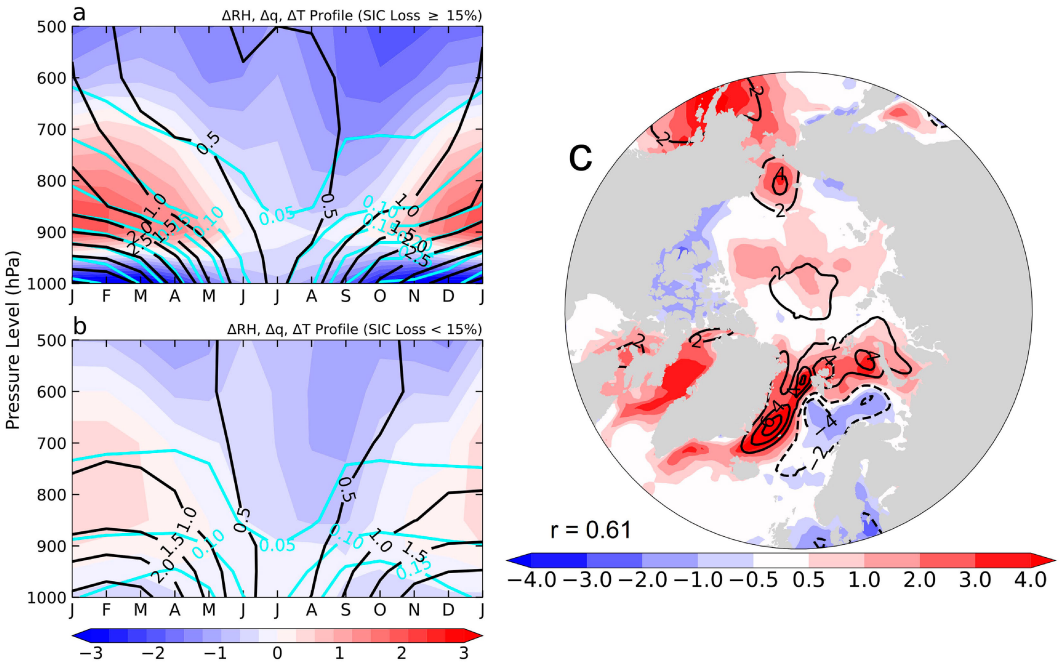

FIG. 7. Arctic (67°–90°N) monthly mean changes (years 1990–2019 minus years 1950–79) in ERA5 relative humidity (%; shading), specific humidity (g kg^{-1}; cyan contours), and air temperature (°C; black contours) averaged over the oceanic areas with (a) SIC loss ≥ 15% and (b) SIC loss < 15%. (c) Changes in relative humidity (%; shading) and cloud fraction (%; contours) averaged over 900–850 hPa. The pattern correlation between the shaded and contour fields is shown in the bottom-left corner of (c).

correlated with sea ice loss with correlation coefficients of −0.44, −0.59, and −0.62, respectively. Increases in cold season cloud properties were largest off the east coast of Greenland, in the Barents–Kara Seas, the Chukchi Sea, and the Sea of Okhotsk, where there was significant SIC loss. This suggests that sea ice loss is a major control on Arctic cloud changes, but we recognize that the correlation coefficient does not imply causal relationships between sea ice and cloud properties.

Our analysis of the vertical profiles (Fig. 5), seasonal cycles (Figs. 6a–c), and spatial distributions (Figs. 6d–f) of Arctic cloud changes between 1950–79 and 1990–2019 suggests that sea ice loss can greatly influence Arctic cloud property changes. Cloud fraction, cloud LWC, and IWC increased around ~950–700 hPa over regions with significant sea ice loss from September to May. From June to August and over areas with little sea ice loss, changes in cloud properties were negligible. We also found decreased Arctic cloud fraction over regions with significant sea ice loss around 1000–950 hPa mainly from August to May (Fig. 5a). Spatially, the changes in Arctic cloud properties from 900 to 850 hPa were moderately correlated with sea ice loss from 1950–79 to 1990–2019 during October–March, with the largest changes off the east coast of Greenland, in the Barents–Kara Seas, the Chukchi Sea, and the Sea of Okhotsk, where there was more than 15% sea ice loss. In the next section, we analyze specific dynamic and thermodynamic mechanisms that may link sea ice loss to changes in the vertical profiles, seasonal cycles, and spatial patterns of Arctic cloud properties.

5. Mechanisms linking increased Arctic cloud fraction and water content to sea ice loss

Increased relative humidity (RH) implies that the air has moved closer to saturation, favoring cloud formation. Figure 7a shows that over areas with significant sea ice loss, RH increased by ~2%–4% between 950 and 700 hPa but decreased by more than 4% from 1000 to 950 hPa during October–March. This is consistent with the increased cloud fraction between 950 and 700 hPa and decreased cloud fraction between 1000 and 950 hPa over areas with significant sea ice loss (Fig. 5a). A slight RH increase (<1%) occurred over regions with little sea ice loss between 950 and 700 hPa (Fig. 7b). The RH profile changed little from May to August over regions with and without sea ice loss. Spatially, changes in RH around 900–850 hPa are strongly correlated with cloud fraction changes (r = 0.61) around 900–850 hPa. We found that cloud fraction increased by ~2%–4% in the Norwegian Sea, Barents–Kara Seas, and Chukchi Sea where RH increased. Further, the RH around 900–850 hPa decreased near the coast of Norway and Sweden in the North Atlantic Ocean, which may partially explain suppressed cloud fraction (Figs. 6d and 7c), and cloud LWC (Fig. 6e) and IWC (Fig. 6f) in this area. We note that more work is required to understand this slight decrease in cloud fraction and water content in the Atlantic sector and is not the focus of this study.

Figure 7a shows that the changes in air temperature and specific humidity over areas with significant sea ice loss were largest during October–March near the surface and they

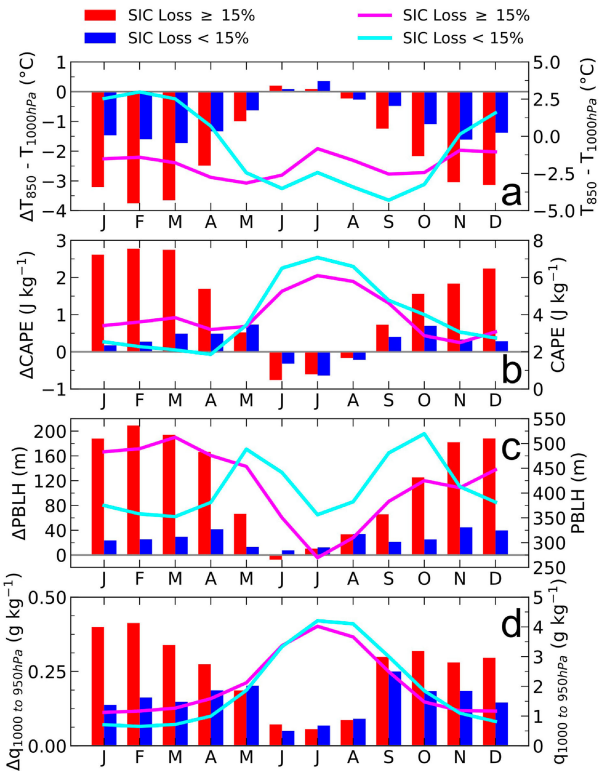

FIG. 8. Long-term changes (bars; left *y* axis; years 1990–2019 minus 1950–79) in ERA5 (a) $T_{850\text{hPa}}$ minus $T_{1000\text{hPa}}$ difference (in °C), (b) convective available potential energy (CAPE; in J kg^{-1}), (c) planetary boundary layer height (PBLH; in m), and (d) 1000 to 950 hPa mean specific humidity (in g kg^{-1}) averaged over regions with 15% or greater SIC loss (red bars) and regions with less than 15% SIC loss (blue bars) poleward of 67°N. The corresponding 1950–79 mean seasonal cycle for each variable averaged over areas with 15% or greater SIC loss (red line) and areas with less than 15% SIC loss (blue line) is shown on the right *y* axis.

weakened with height, consistent with the bottom-heavy warming profiles for the Arctic cold season shown previously (Jenkins and Dai 2022). Atmospheric warming and moistening were weak from May to August and over areas with little sea ice loss (Fig. 7b). The large warming from 1000 to 950 hPa over regions with significant sea ice loss increased the saturation specific humidity and thus decreased the RH and cloud fraction there. From 950 to 700 hPa, the effect of atmospheric moistening outpaced the effect of warming, leading to increased RH and thus cloud fraction. Enhanced vertical motions over areas with significant sea ice loss (e.g., Fig. 10a) transport moisture away from the near-surface layer to the layer around 950–700 hPa, decreasing (increasing) the RH near the surface (around 950–700 hPa). The lack of strong warming and moistening during the summer months produces small (i.e., <1%) RH changes (Fig. 7a), thus resulting in small changes in cloud properties during the warm season (Figs. 6a–c).

Figure 8a shows the 1950–79 climatology and long-term changes of the Arctic lower-tropospheric temperature inversion (i.e., $T_{850\text{hPa}} - T_{1000\text{hPa}}$). We note that the $T_{850\text{hPa}} - T_{1000\text{hPa}}$ inversion in ERA5 is underestimated relative to observations, but that ERA5 reproduces the general structure of the Arctic temperature profile well (Graham et al. 2019a) and simulates atmospheric conditions better than other reanalysis datasets (Graham et al. 2019b). The Arctic mean temperature profile is stable with a temperature inversion over areas with little sea ice loss from November to April. A stable profile with a strong lower-tropospheric temperature inversion would suppress vertical mixing between the surface and lower troposphere and result in weak vertical transfer of moisture and energy. From 1950–79 to 1990–2019, the strength of the Arctic lower-tropospheric temperature inversion decreased in all but the summer months, especially over regions with significant sea ice loss (Fig. 8a). This suggests that enhanced surface warming induced by sea ice loss weakens Arctic lower-tropospheric stability, thus favoring an environment for enhanced vertical motion and mixing. To demonstrate that, we further show the climatology and changes in convective available potential energy (CAPE; Fig. 8b) and planetary boundary layer height (PBLH; Fig. 8c) over the Arctic. The 1950–79 CAPE climatology shows a similar seasonal cycle with peak positive CAPE in summer over areas with and without significant sea ice loss. CAPE increased by ~2–2.75 J kg^{-1} (~100% of the 1950–79 climatology) during October–March over areas with significant sea ice loss, compared to a less than 1 J kg^{-1} increase over areas with little sea ice loss (Fig. 8b). The PBLH increase was also largest (~120–200 m) during October–March over areas with significant sea ice loss (Fig. 8c). The reduced temperature inversion, increased CAPE, PBLH, and near-surface specific humidity (Fig. 8d) over areas with significant sea ice loss suggest that warming associated with Arctic sea ice loss increased vertical transport of moisture and energy from the surface layer to lower troposphere, favoring increased RH and enhanced cloud formation from ~950 to 700 hPa.

The spatial distributions of the October–March CAPE (Fig. 9b) and PBLH (Fig. 9c) changes correspond strongly to the patterns of sea ice loss with correlation coefficients −0.71, and −0.87, respectively. The temperature inversion change patterns were also correlated with the sea ice loss (r = 0.48; Fig. 9a). Over areas with significant sea ice loss, the temperature inversion weakened by −3° to −4°C and slightly decreased by −1° to −2°C over the central Arctic region where less than 5% SIC loss occurred (Fig. 9a). Similarly, changes in cold-season CAPE (Fig. 9b) and PBLH (Fig. 9c) were localized over areas with large sea ice loss, with the largest increases near the east coast of Greenland, the Barents–Kara Sea, the Sea of Okhotsk, and the Chukchi Sea. The temperature inversion changed little during April–September but exhibited a moderate pattern correlation with sea ice loss (r = 0.56; Fig. 9d). Further, the April–September spatial patterns of CAPE (Fig. 9e) and PBLH (Fig. 9f) changes were weakly correlated with sea ice changes, with correlation coefficients of 0.12 and −0.42, respectively. Our analyses suggest that sea ice loss, which enhances winter surface warming (Deser et al. 2010; Dai et al. 2019), can lead to reduced temperature inversion, increased vertical mixing, and higher CAPE and PBLH

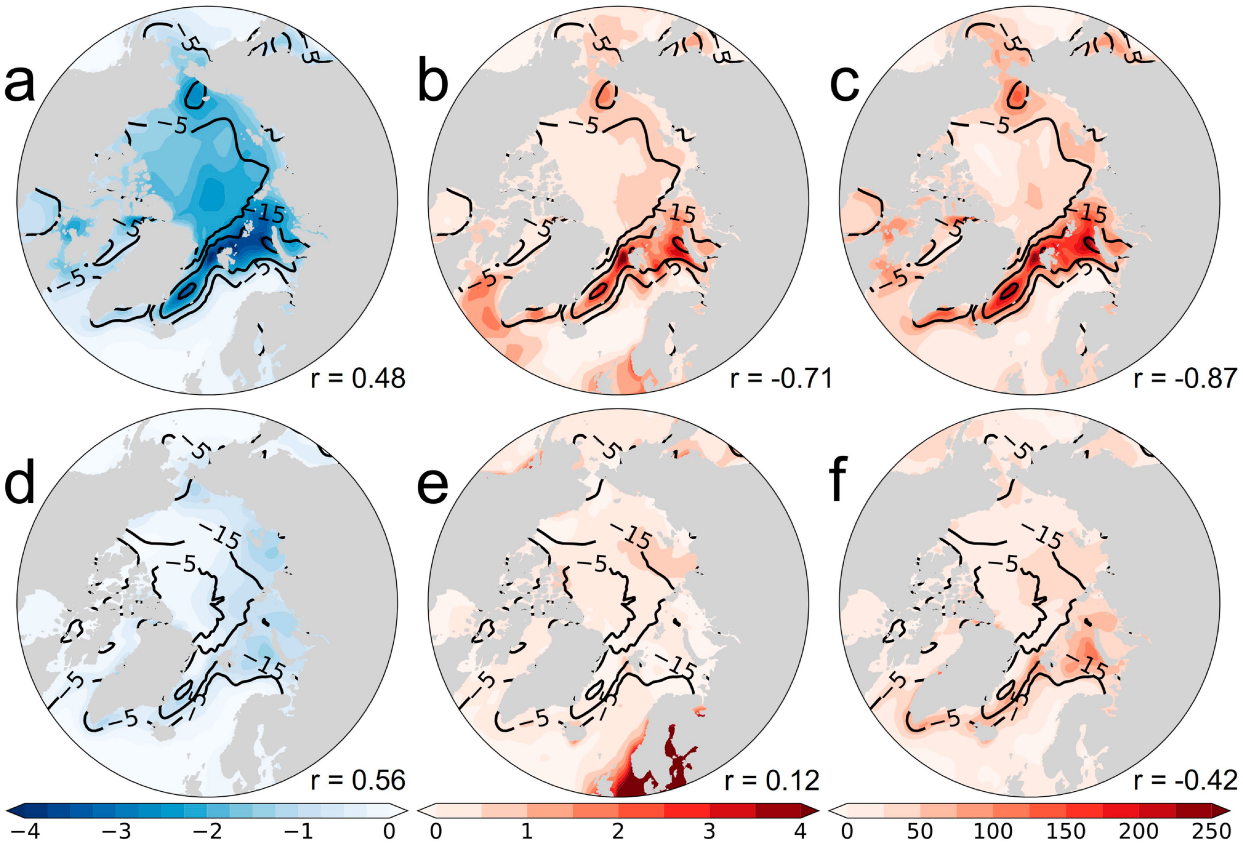

FIG. 9. Long-term changes (years 1990–2019 minus years 1950–79) in ERA5 sea ice concentration (contours; %; the −5%, −15%, and −30% levels are shown) and (a),(d) $T_{850hPa} - T_{1000hPa}$ difference (shading; °C), (b),(e) CAPE (shading; J kg^{-1}), and (c),(f) PBLH (shading; m) for (a)–(c) October–March and (d)–(f) April–September. The pattern correlation between the shaded and contour field is shown in the bottom-right corner of each panel. All the correlation coefficients have a p value less than 0.01.

during October–March, while the influence is small in the warm season.

Figure 10 shows the climatology and changes in the profiles of vertical velocity and horizontal wind divergence. The 1950–79 mean vertical velocity was upward during October–March, with a magnitude of −12 to −16 Pa s^{-1} (−8 to −12 Pa s^{-1}) over regions with ≥15% (<15%) SIC loss. During May–August, the 1950–79 mean vertical velocity was near-zero over both surface types (Figs. 10a,b). Over areas with significant sea ice loss, upward motion was enhanced in the lower troposphere (i.e., 950–800 hPa) during October–March by -8×10^{-3} Pa s^{-1}, while the changes during May–September were negligible (Fig. 10a). Without significant sea ice loss, vertical velocity changed little for all months from the surface to 500 hPa (Fig. 10b). The spatial patterns of the cold-season vertical velocity changes from 950 to 700 hPa show enhanced upward motion east of Greenland and in the Barents–Kara Seas, with small increases in upward motion in the Chukchi Sea (Fig. 11a). Upward vertical velocity increased most over areas with large sea ice loss during the cold season, although the two only show a weak pattern correlation (r = 0.18) (Fig. 11a). April–September experienced little change in vertical velocity and its changes did not spatially correspond with sea ice loss (r = 0.07; Fig. 11b). The warming associated with sea ice loss likely enhanced upward vertical motions from 1950–79 to 1990–2019 by making the air near the surface more buoyant. Further, enhanced upward atmospheric motions over newly exposed ocean water surfaces would lead to increased upward transport of energy and moisture and enhanced cloud fraction and water content from 950 to 700 hPa.

We further examine the vertical profiles (Figs. 10c,d) and spatial patterns (Fig. 12) of horizontal wind divergence, which is related to the vertical gradient of the vertical velocity so that a horizontal convergence of airmass would lead to a vertical divergence of airmass. Over both areas with (Fig. 10c) and without (Fig. 10d) significant SIC loss, the 1950–79 climatological conditions show mean convergence near the surface (i.e., 1000–800 hPa) and mean divergence in the layer ~800–600 hPa (Figs. 10c,d), consistent with the decrease in upward velocity with height below ~800 hPa (Figs. 10a,b). With less than 15% sea ice loss the divergence profile experienced minimal changes throughout the year (Fig. 10d). In regions with significant SIC loss, the low-level (1000–950 hPa) convergence increased by $\sim -8 \times 10^{-7}$ s^{-1} during October–March while the change aloft (~900–700 hPa) was a divergence of

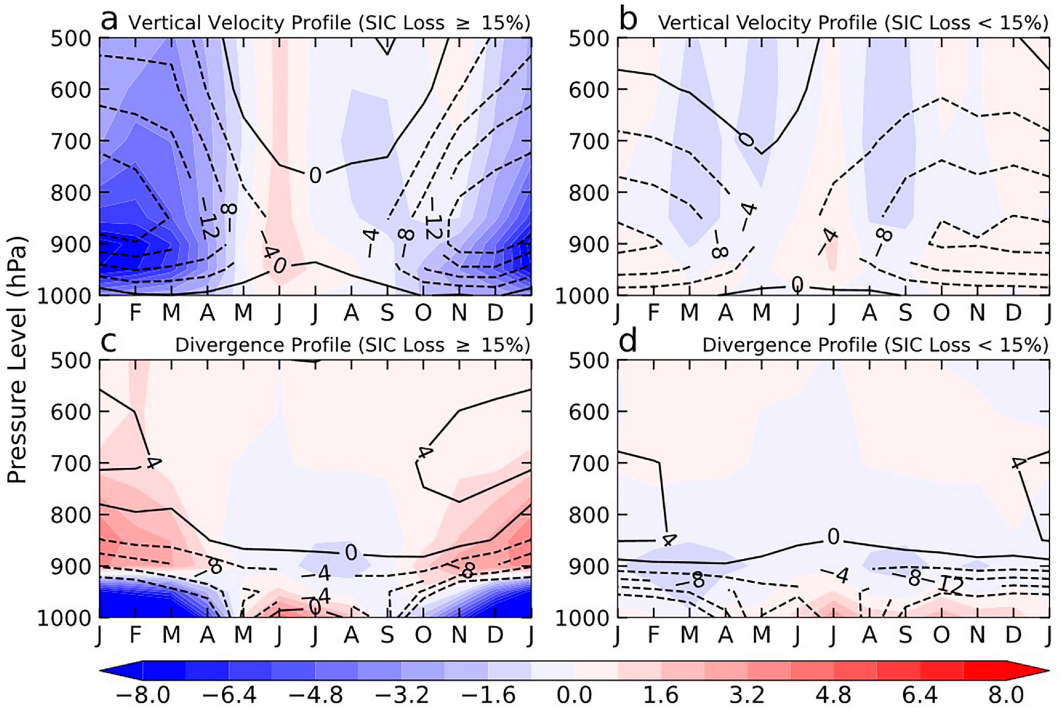

FIG. 10. Arctic (67°–90°N) monthly mean climatology (years 1950–79; contours) and changes (years 1990–2019 minus 1950–79; shading) in ERA5 (a),(b) vertical velocity (in mPa s^{-1}; negative upward) and (c),(d) horizontal wind divergence (in $s^{-1} \times 10^{-7}$) averaged over the oceanic areas (a),(c) with 15% or greater SIC loss and (b),(d) with less than 15% SIC loss.

~2–5 × 10^{-7} s^{-1}, which weakened the mean convergence below ~800 hPa but enhanced the divergence above (Fig. 10c). We also note that from May to August there is a positive divergence change around 1000–950 hPa, which should weaken the climatological convergence during these months (Fig. 10c). The change patterns of the divergence fields averaged over 1000–950 hPa (Fig. 12a) and 900–850 hPa (Fig. 12b) confirm that areas with 15% or greater sea ice loss experienced

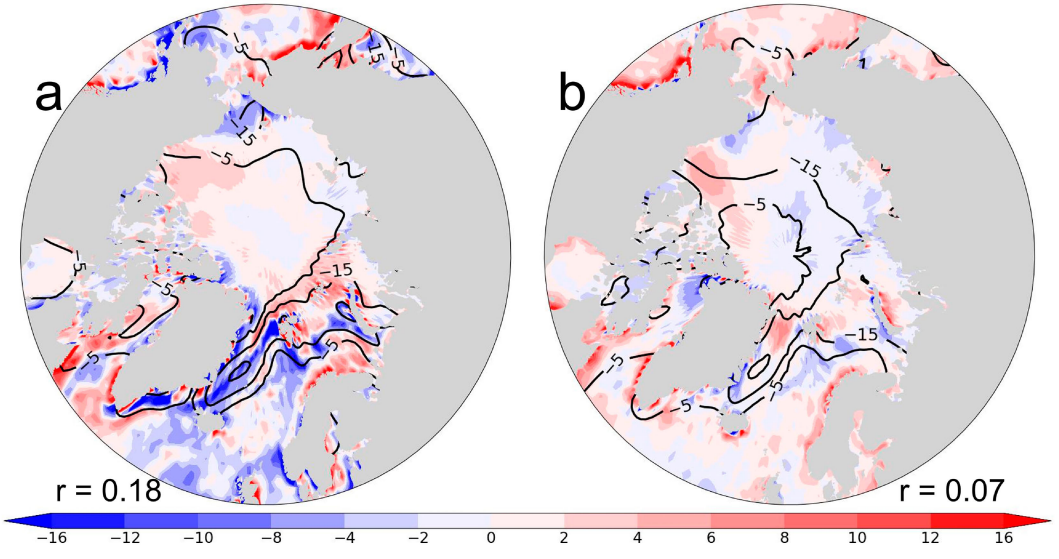

FIG. 11. Long-term changes (years 1990–2019 minus 1950–79) in ERA5 vertical velocity (in mPa s^{-1}; shading) averaged over 950–700 hPa and sea ice concentration (%; contours) for (a) October–March and (b) April–September. The pattern correlation between the divergence and sea ice change fields is shown in the bottom corner of each panel. Each correlation has a p value less than 0.01.

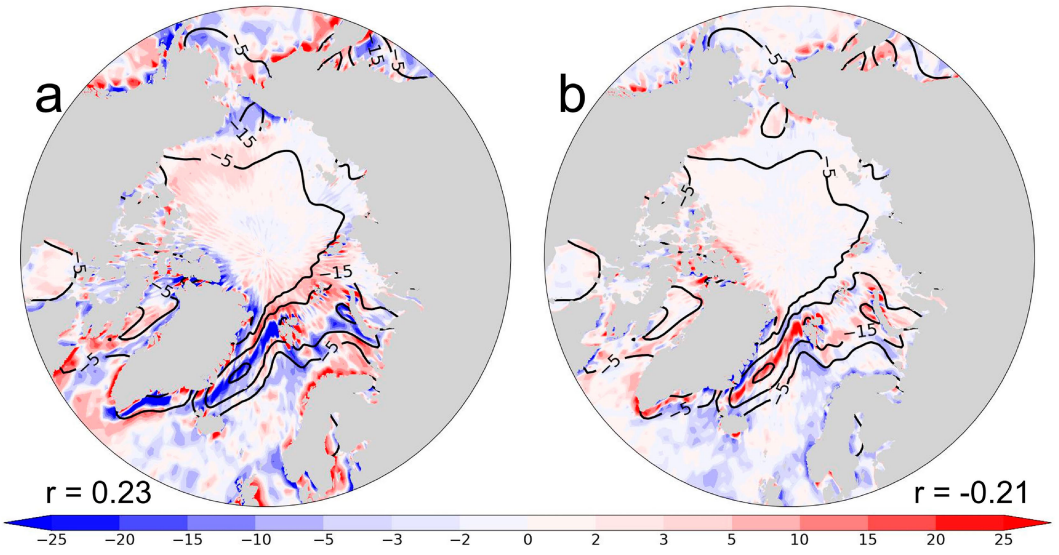

FIG. 12. Long-term changes (years 1990–2019 minus 1950–79) in ERA5 horizontal divergence (in $s^{-1} \times 10^{-7}$; shading) averaged over (a) 1000–950 and (b) 900–850 hPa for October–March. Contours represent the change in sea ice concentration for years 1990–2019 minus years 1950–79. The pattern correlation between the divergence and sea ice change fields is shown in the bottom corner of each panel. Each correlation has a p value less than 0.01.

enhanced near-surface convergence ($r = 0.23$; Fig. 12a) and strengthened divergence aloft ($r = -0.21$; Fig. 12b). Note the striking alignment of the convergence (divergence) change from 1000 to 950 hPa (900–850 hPa) between Greenland and Svalbard.

Changes in moisture divergence, precipitation, and surface evaporation

We conduct a brief analysis of the spatial patterns of the mean vertically integrated horizontal moisture divergence (Figs. 13a,d), precipitation, and surface evaporation (Fig. 14) to further reveal how sea ice loss affects clouds through the surface water fluxes. The changes in moisture divergence exhibit strong negative spatial correlation with sea ice changes during October–March ($r = -0.68$; Fig. 13a), but the correlation is weak during April–September ($r = -0.19$; Fig. 13d). Further, the largest increases in moisture divergence occurred over areas with 15% or greater sea ice loss (Fig. 13a) during October–March with an increase of 0.3–0.7 mm day^{-1}. The enhancement of moisture divergence was largest near Greenland and Svalbard, followed by the Chukchi Sea and Sea of Okhotsk. This suggests that atmospheric motions tended to decrease atmospheric moisture content over areas with sea ice retreat during October–March.

We next examine the change patterns in surface evaporation (Figs. 14a,c), precipitation (Figs. 14b,d), and evaporation minus precipitation ($E - P$; Figs. 13b,e), and their relationship to sea ice loss. Evaporation (Fig. 14a) and precipitation (Fig. 14b) are closely related to sea ice loss during October–March ($r = -0.87$ and $r = -0.52$). Lack of ocean–atmosphere coupling during April–September produced weak or no correlation between surface evaporation ($r = -0.34$; Fig. 14c) or precipitation ($r = 0.02$; Fig. 14d) and sea ice changes. We notice that October–March precipitation increases nearly everywhere under rising temperatures, with some enhancement over areas with significant sea ice loss (Fig. 14b). In contrast, changes in evaporation were localized over sea ice loss regions during October–March (Fig. 14a). Notably, $E - P$ exhibits a strong negative correlation with sea ice loss during October–March ($r = -0.71$; Fig. 13b), but this relationship weakens during April–September ($r = -0.28$; Fig. 13e). Over regions with sea ice loss, surface evaporation exceeded the total precipitation by ~0.3–0.7 mm day^{-1}, implying net moistening of the atmosphere through surface water fluxes during the cold season in sea ice retreat areas (Fig. 13b). The net increase in surface evaporation and moisture divergence suggests that surface water fluxes, rather than remote moisture transport, are a key moisture source for enhanced Arctic cloudiness during the cold season. The differences between the changes in moisture flux divergence and changes in $E - P$ fields are approximately zero over most areas of the Arctic for both October–March (Fig. 13c) and April–September (Fig. 13f), suggesting that net increases in surface moisture fluxes are balanced by atmospheric moisture divergence, as changes in atmospheric water storage are relatively small.

One may argue that there is a net increase in remote atmospheric moisture input into the Arctic and that the enhanced moisture is redistributed into the spatial patterns shown in Figs. 13 and 14. In Figs. 15 and 16, we show the zonal-mean changes in meridional moisture transport (Figs. 15b–d) and vertically integrated northward water vapor flux (Fig. 16). In

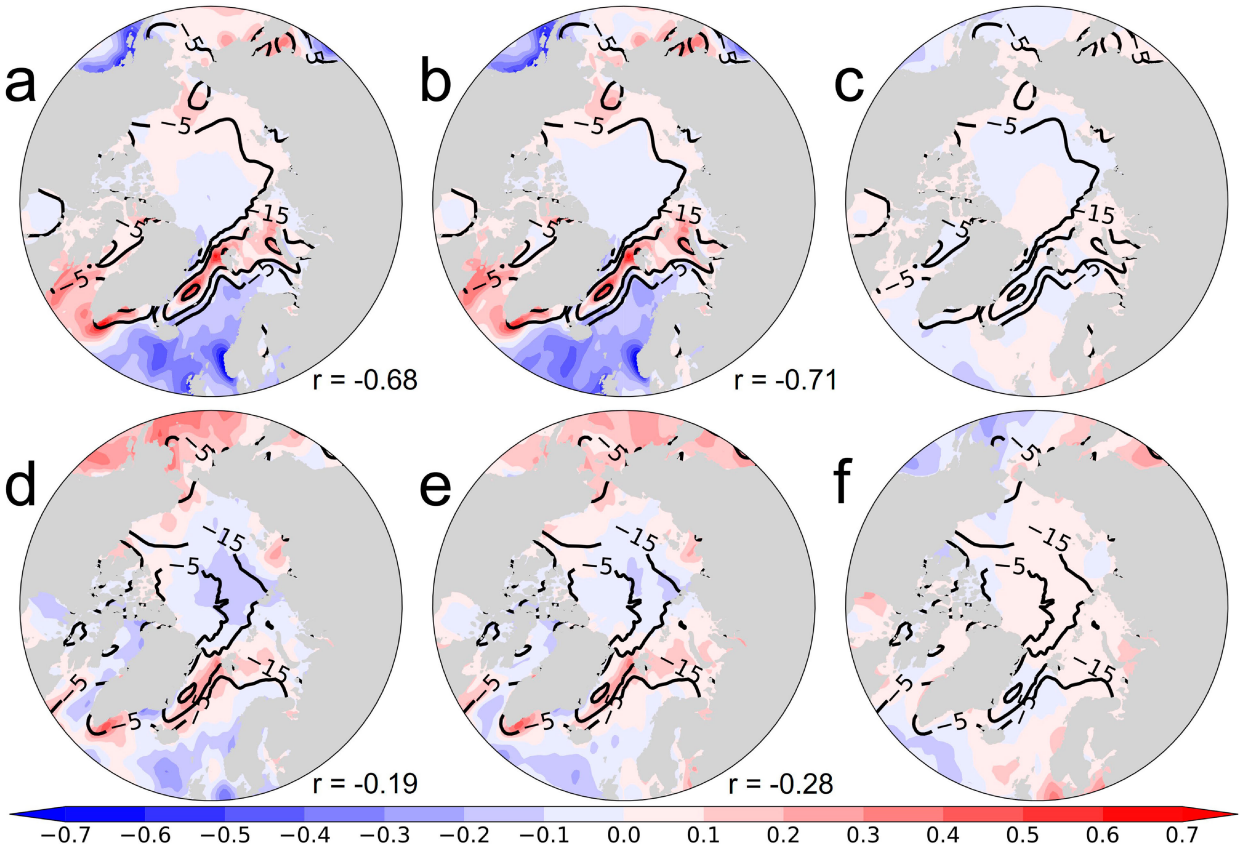

FIG. 13. Long-term changes (years 1990–2019 minus years 1950–79) in ERA5 sea ice concentration (contours; %; the −5%, −15%, and −30% levels are shown) and (a),(d) vertically integrated atmospheric moisture flux divergence (shading; in mm day^{-1}), (b),(e) evaporation minus precipitation ($E - P$; shading; mm day^{-1}), and (c),(f) their difference for (a)–(c) October–March and (d)–(f) April–September. The pattern correlation between the shaded and contour field is shown in the bottom-right corner of (a), (b), (d), and (e). Each correlation coefficient has a p value less than 0.01.

the annual mean and during April–September, there is a net increase in meridional moisture transport at all latitudes in the Arctic (Fig. 16) from ~1000 to 800 hPa (Figs. 15b,d). During October–March, there is a decrease in the vertically integrated northward water vapor flux (Fig. 16) and meridional moisture transport (Fig. 15c) across ~70°–77°N, where cold season sea ice loss is largest (Fig. 15a). Thus, remote moisture transport plays a key role in moistening the Arctic during April–September but weakens over latitudes where there is large sea ice loss during October–March. This further suggests that enhanced evaporation from exposed water surfaces plays a key role in moistening the Arctic boundary layer in the cold season.

6. Summary and discussion

a. Summary

To examine how sea ice loss may affect clouds in the Arctic, we analyzed the long-term changes from 1950–79 to 1990–2019 in sea ice concentration (SIC), cloud fraction, cloud liquid and ice water contents, and other surface and atmospheric fields using ERA5 data. We first made a comparison of ERA5 cloud fields and cloud radiative forcing (CRF) data with CERES satellite data from January 2001 to December 2020. ERA5 produces more clouds over sea ice relative to satellite observations although the MODIS clouds used in CERES may be underestimated, especially in winter (Liu et al. 2010). Net CRF agrees well between reanalysis and CERES data; however, ERA5 radiation fields may be tuned to correct for biases or deficiencies in radiation fields. We emphasize that the physical processes revealed using ERA5 data provide useful insights into how sea ice loss may influence Arctic clouds, despite the potential biases and deficiencies in ERA5 cloud fields. The difference in mean cloud distribution between ERA5 and CERES clouds for years 2001–20 does not imply that the long-term changes in Arctic clouds are incorrect in ERA5. Further, the lack of in situ observations of clouds in the central Arctic region makes evaluating ERA5 and satellite-based Arctic cloud fields challenging.

The ERA5 data show that Arctic cloud fraction and cloud liquid and ice water contents around ~950–700 hPa increased from 1950–79 to 1990–2019 over areas with significant

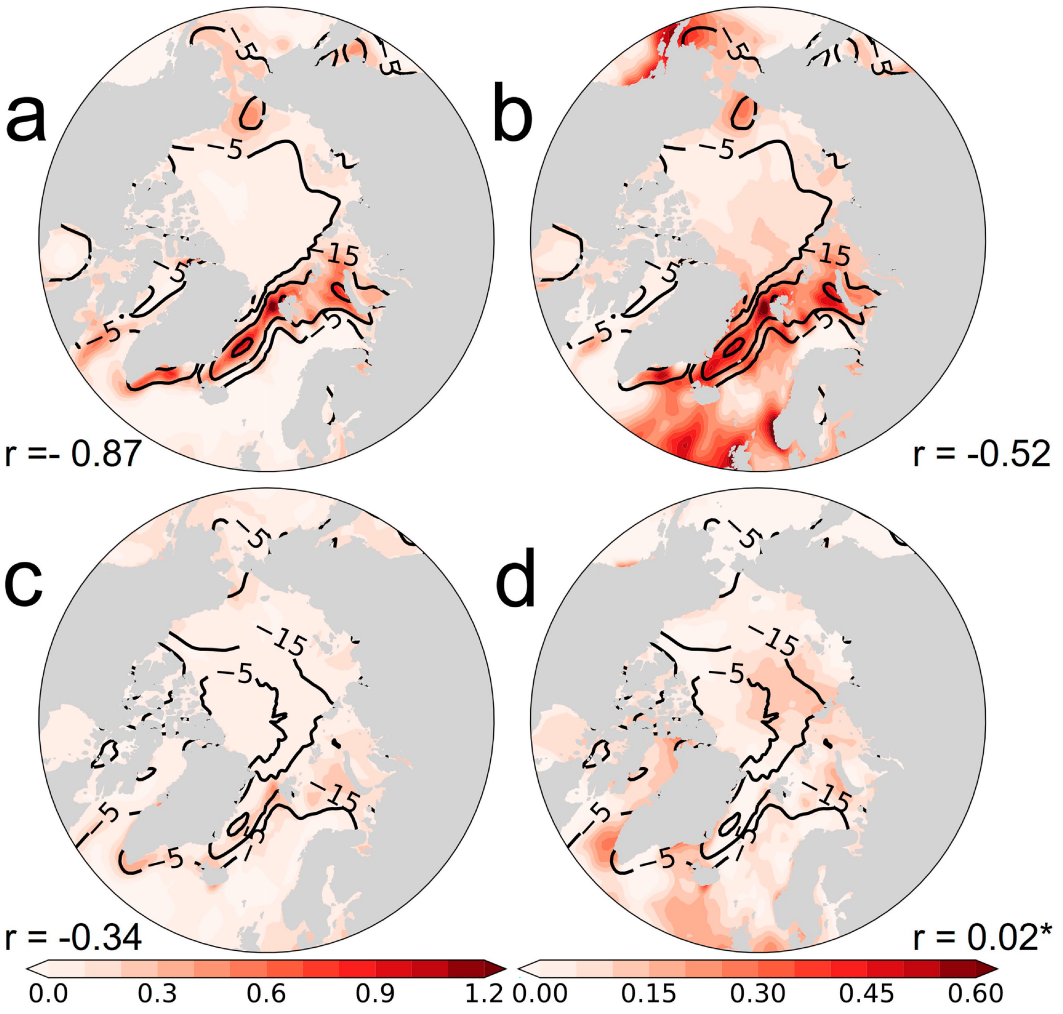

FIG. 14. Long-term changes (years 1990–2019 minus years 1950–79) in ERA5 sea ice concentration (contours; %; the −5%, −15%, and −30% levels are shown) and (a),(c) evaporation (E; shading; left color bar; mm day^{-1}) and (b),(d) precipitation (P; shading; right color bar; mm day^{-1}) for (a),(b) October–March and (c),(d) April–September. The pattern correlation between the shaded and contour field is shown in the bottom-right corner of each panel. Each correlation coefficient has a p value less than 0.01 except for the case in (d).

(≥15%) sea ice loss, while cloud fraction around 1000–950 hPa decreased during October–March. Negligible changes in cloud properties occurred over areas with little (<15%) sea ice loss or during April–September. Atmospheric warming and moistening was strongest in autumn and winter near the surface but was weak during summer. Large surface warming increased the saturation specific humidity of the near-surface layer more than its actual specific humidity, whose rate of increase may be partially counteracted by enhanced upward export of moisture. This imbalance in the rate of increase between saturation and actual specific humidity resulted in a decrease in the RH and cloud amount around 1000–950 hPa. From ~950 to 700 hPa where warming was weaker than near the surface, the atmosphere experienced a net moistening (as indicated by the increased RH) likely due to increased upward moisture transport, leading to enhanced cloud amount and cloud water content there. The RH changed little during the summer season or over areas with little sea ice loss. During the cold season, atmospheric moisture divergence, which is a measure of surface $E - P$ flux, increased over the areas with significant sea ice loss from 1950–79 to 1990–2019. We also show that the long-term change in meridional moisture transport is equatorward along latitudes with large cold-season sea ice loss. This suggests that increased local surface evaporation, rather than remote moisture transport, provides a key moisture source for increased cloudiness over newly exposed ocean water surfaces in winter.

b. Discussion

Our results using ERA5 data showed that sea ice loss is associated with increased cloud fraction and cloud water content during Arctic autumn and winter, consistent with

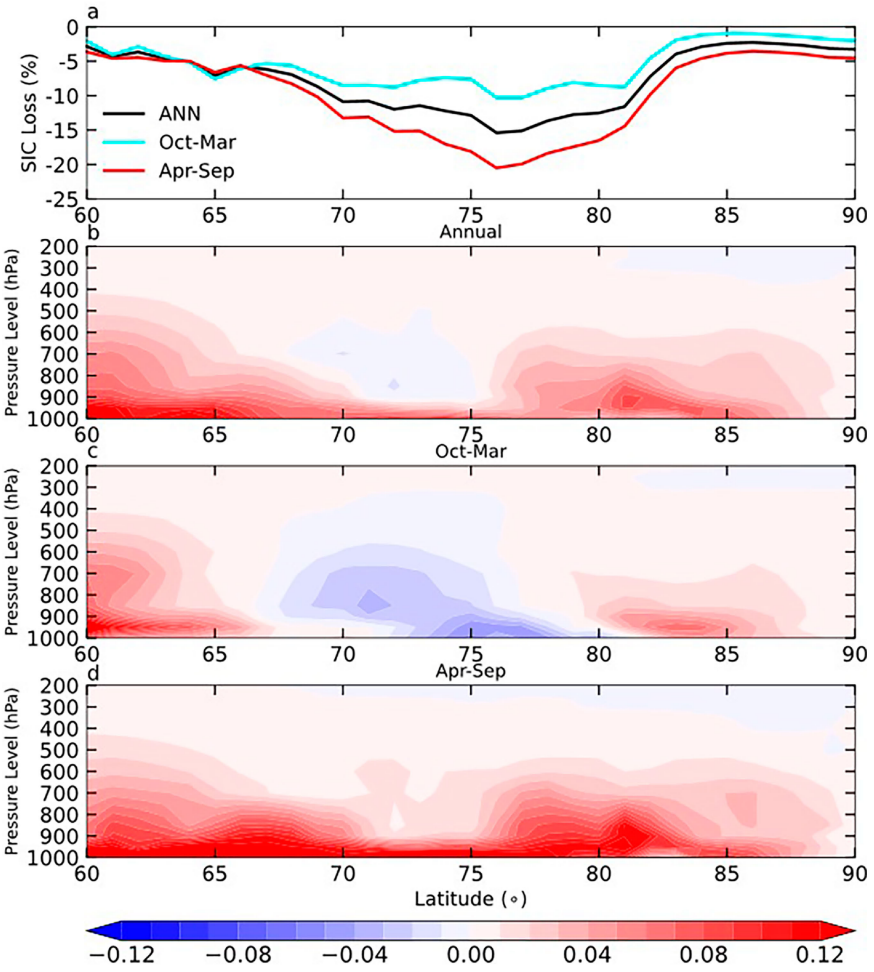

FIG. 15. Zonal-mean changes in (a) sea ice concentration (in %), and (b)–(d) vertical profiles of meridional moisture transport ($\mathbf{vq}$; in g kg^{-1} m s^{-1}) for the (b) annual, (c) October–March, and (d) April–September mean.

previous studies (e.g., Kay and Gettelman 2009; Palm et al. 2010; Morrison et al. 2019). This study makes a novel contribution to this general topic by analyzing the long-term changes (i.e., the difference between two 30-yr periods), rather than by examining variations and trends over shorter periods (i.e., 20 years or less) as done previously (Schweiger et al. 2008; Kay and Gettelman 2009; Palm et al. 2010; Morrison et al. 2018). The difference between years 1950–79 and years 1990–2019 estimates the effects of GHG-induced warming and long-term sea ice loss on Arctic cloud changes and atmospheric conditions; however, internal variability may also contribute to these differences (Wettstein and Deser 2014). Further, we show new dynamic and thermodynamic processes that explain why regions with sea ice loss are more prone to enhanced cloudiness than ice-covered regions. Specifically, we analyzed the seasonality and spatial patterns of changes in CAPE and divergence fields that have not been examined in previous studies. We also show that local surface evaporation provides an essential source of moisture for enhanced cloudiness associated with sea ice loss. To our knowledge, the long-term changes in local evaporation and meridional moisture flux have not been thoroughly examined.

We recognize that clouds are influenced not only by conditions of the underlying surface, but also by the background meteorological conditions (Barton and Veron 2012; Taylor et al. 2015). Our composite analyses for areas with and without large sea ice loss minimize the effects of other factors. Further, cloud anomalies can also affect surface conditions, including sea ice loss. Thus, the SIC–cloud interactions are two-way and our correlation analysis cannot untangle the causal relationship between Arctic sea ice loss and cloud changes. For this reason, we recommend analysis of climate model simulations to further assess the causal relationship between sea ice loss and clouds. Nevertheless, our results, together with previous studies (e.g., Deser et al. 2010; Screen and Simmonds 2010a,b; Dai et al. 2019), have shown that sea ice loss can increase oceanic heat and water fluxes into the atmosphere during the cold season, leading to large surface warming and increased upward heat and

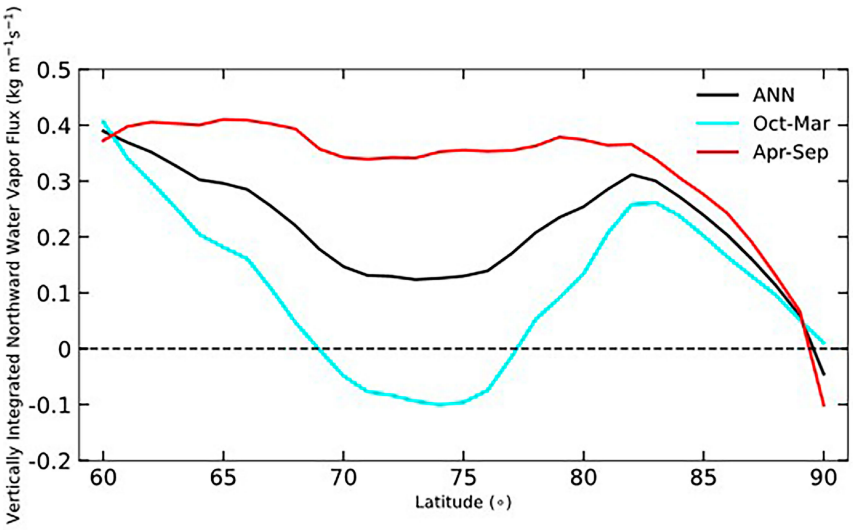

FIG. 16. Zonal-mean change in the vertically integrated northward water vapor flux for the annual (black line), October–March (cyan line), and April–September (red line) mean.

moisture transport from the surface layer into the layer above. Thus, from this perspective, we interpreted the cloud differences between the areas with and without significant sea ice loss as a response to sea ice loss.

Acknowledgments. The authors acknowledge the National Science Foundation (Grants AGS-2015780 and OISE-1743738) for supporting this work and three anonymous reviewers who provided constructive feedback to improve the manuscript. The National Center for Atmospheric Research is sponsored by the National Science Foundation.

Data availability statement. The ERA5 data used in this study may be downloaded from https://cds.climate.copernicus.eu/#!/search?text=ERA5&type=dataset. The CERES data are available from https://ceres.larc.nasa.gov/data/.

REFERENCES

Abe, M., T. Nozawa, T. Ogura, and K. Takata, 2016: Effect of retreating sea ice on Arctic cloud cover in simulated recent global warming. *Atmos. Chem. Phys.*, **16**, 14 343–14 356, https://doi.org/10.5194/acp-16-14343-2016.

Alkama, R., P. C. Taylor, L. G.-S. Martin, H. Douville, G. Duveiller, G. Forzieri, D. Swingedouw, and A. Cescatti, 2020: Clouds damp the radiative impacts of polar sea ice loss. *Cryosphere*, **14**, 2673–2686, https://doi.org/10.5194/tc-14-2673-2020.

Barton, N. P., and D. E. Veron, 2012: Response of clouds and surface energy fluxes to changes in sea-ice cover over the Laptev Sea (Arctic Ocean). *Climate Res.*, **54**, 69–84, https://doi.org/10.3354/cr01101.

Bell, B., and Coauthors, 2021: The ERA5 global reanalysis: Preliminary extension to 1950. *Quart. J. Roy. Meteor. Soc.*, **147**, 4186–4227, https://doi.org/10.1002/qj.4174.

Boeke, R. C., and P. C. Taylor, 2018: Seasonal energy exchange in sea ice retreat regions contributes to differences in projected Arctic warming. *Nat. Commun.*, **9**, 5017, https://doi.org/10.1038/s41467-018-07061-9.

Burt, M. A., D. A. Randall, and M. D. Branson, 2016: Dark warming. *J. Climate*, **29**, 705–719, https://doi.org/10.1175/JCLI-D-15-0147.1.

Ceppi, P., F. Brient, M. D. Zelinka, and D. L. Hartmann, 2017: Cloud feedback mechanisms and their representation in global climate models. *Wiley Interdiscip. Rev.: Climate Change*, **8**, e465, https://doi.org/10.1002/wcc.465.

Choi, Y.-S., B.-M. Kim, S.-K. Hur, S.-J. Kim, J.-H. Kim, and C.-H. Ho, 2014: Connecting early summer cloud-controlled sunlight and late summer sea ice in the Arctic. *J. Geophys. Res. Atmos.*, **119**, 11 087–11 099, https://doi.org/10.1002/2014JD022013.

Cox, C. J., T. Uttal, C. N. Long, M. D. Shupe, R. S. Stone, and S. Starkweather, 2016: The role of springtime Arctic clouds in determining autumn sea ice extent. *J. Climate*, **29**, 6581–6596, https://doi.org/10.1175/JCLI-D-16-0136.1.

Curry, J. A., J. L. Schramm, W. B. Rossow, and D. Randall, 1996: Overview of Arctic cloud and radiation characteristics. *J. Climate*, **9**, 1731–1764, https://doi.org/10.1175/1520-0442(1996)009<1731:OOACAR>2.0.CO;2.

Cuzzone, J., and S. Vavrus, 2011: The relationships between Arctic sea ice and cloud-related variables in the ERA-Interim reanalysis and CCSM3. *Environ. Res. Lett.*, **6**, 014016, https://doi.org/10.1088/1748-9326/6/1/014016.

Dai, A., D. Luo, M. Song, and J. Liu, 2019: Arctic amplification is caused by sea-ice loss under increasing CO_2. *Nat. Commun.*, **10**, 121, https://doi.org/10.1038/s41467-018-07954-9.

Deser, C., R. Tomas, M. Alexander, and D. Lawrence, 2010: The seasonal atmospheric response to projected Arctic sea ice loss in the late twenty-first century. *J. Climate*, **23**, 333–351, https://doi.org/10.1175/2009JCLI3053.1.

Doelling, D. R., M. Sun, L. T. Nguyen, M. L. Nordeen, C. O. Haney, D. F. Keyes, and P. E. Mlynczak, 2016: Advances in geostationary-derived longwave fluxes for the CERES synoptic (SYN1-deg) product. *J. Atmos. Oceanic Technol.*, **33**, 503–521, https://doi.org/10.1175/JTECH-D-15-0147.1.

Eastman, R., and S. G. Warren, 2010: Interannual variations of Arctic cloud types in relation to sea ice. *J. Climate*, **23**, 4216–4232, https://doi.org/10.1175/2010JCLI3492.1.

England, M. R., I. Eisenmann, N. J. Lutsko, and T. J. W. Wagner, 2021: The recent emergence of Arctic amplification. *Geophys. Res. Lett.*, **48**, e2021GL094086, https://doi.org/10.1029/2021GL094086.

Gettelman, A., and S. C. Sherwood, 2016: Processes responsible for cloud feedback. *Curr. Climate Change Rep.*, **2**, 179–189, https://doi.org/10.1007/s40641-016-0052-8.

Graham, R. M., and Coauthors, 2019a: Evaluation of six atmospheric reanalyses over Arctic sea ice from winter to early summer. *J. Climate*, **32**, 4121–4143, https://doi.org/10.1175/JCLI-D-18-0643.1.

——, S. R. Hudson, and M. Maturilli, 2019b: Improved performance of ERA5 in Arctic gateway relative to four global atmospheric reanalyses. *Geophys. Res. Lett.*, **46**, 6138–6147, https://doi.org/10.1029/2019GL082781.

Hersbach, H., and Coauthors, 2020: The ERA5 global reanalysis. *Quart. J. Roy. Meteor. Soc.*, **146**, 1999–2049, https://doi.org/10.1002/qj.3803.

Hirahara, S., M. A. Balmaseda, E. de Boisseson, and H. Hersbach, 2016: Sea surface temperature and sea ice concentration for ERA5. ERA Rep. Series 26, 27 pp., https://www.ecmwf.int/sites/default/files/elibrary/2016/16555-sea-surface-temperature-and-sea-ice-concentration-era5.pdf.

Huang, Y., and Coauthors, 2019: Thicker cloud and accelerated Arctic sea ice decline: The atmosphere-sea ice interactions in spring. *Geophys. Res. Lett.*, **46**, 6980–6989, https://doi.org/10.1029/2019GL082791.

Intrieri, J. M., M. D. Shupe, T. Uttal, and B. J. McCarty, 2002a: An annual cycle of Arctic cloud characteristics observed by radar and lidar at SHEBA. *J. Geophys. Res.*, **107**, 8030, https://doi.org/10.1029/2000JC000423.

——, C. W. Fairall, M. D. Shupe, P. O. G. Persson, E. L. Andreas, P. S. Guest, and R. E. Moritz, 2002b: An annual cycle of Arctic surface cloud forcing at SHEBA. *J. Geophys. Res.*, **107**, 8039, https://doi.org/10.1029/2000JC000439.

Jenkins, M., and A. Dai, 2021: The impact of sea-ice loss on Arctic climate feedbacks and their role for Arctic amplification. *Geophys. Res. Lett.*, **48**, e2021GL094599, https://doi.org/10.1029/2021GL094599.

——, and ——, 2022: Arctic climate feedbacks in ERA5 reanalysis: Seasonal and spatial variations and the impact of sea-ice loss. *Geophys. Res. Lett.*, **49**, e2022GL099263, https://doi.org/10.1029/2022GL099263.

Kapsch, M.-L., R. G. Graversen, and M. Tjernström, 2013: Springtime atmospheric energy transport and the control of Arctic summer sea-ice extent. *Nat. Climate Change*, **3**, 744–748, https://doi.org/10.1038/nclimate1884.

Kato, S., and Coauthors, 2018: Surface irradiances of edition 4.0 Clouds and the Earth's Radiant Energy System (CERES) Energy Balanced and Filled (EBAF) data product. *J. Climate*, **31**, 4501–4527, https://doi.org/10.1175/JCLI-D-17-0523.1.

Kay, J. E., and A. Gettelman, 2009: Cloud influence on and response to seasonal Arctic sea ice loss. *J. Geophys. Res.*, **114**, D18204, https://doi.org/10.1029/2009JD011773.

——, T. L'Ecuyer, H. Chepfer, N. Loeb, A. Morrison, and G. Cesana, 2016: Recent advances in Arctic cloud and climate research. *Curr. Climate Change Rep.*, **2**, 159–169, https://doi.org/10.1007/s40641-016-0051-9.

Liu, Y., S. A. Ackerman, B. C. Maddux, J. R. Key, and R. A. Frey, 2010: Errors in cloud detection over the Arctic using a satellite imager and implications for observing feedback mechanisms. *J. Climate*, **23**, 1894–1907, https://doi.org/10.1175/2009JCLI3386.1.

——, J. R. Key, Z. Liu, X. Wang, and S. J. Vavrus, 2012: A cloudier Arctic expected with diminishing sea ice. *Geophys. Res. Lett.*, **39**, L05705, https://doi.org/10.1029/2012GL051251.

Loeb, N. G., and Coauthors, 2018: Clouds and the Earth's Radiant Energy System (CERES) Energy Balanced and Filled (EBAF) top-of-atmosphere (TOA) edition-4.0 data product. *J. Climate*, **31**, 895–918, https://doi.org/10.1175/JCLI-D-17-0208.1.

Monroe, E. E., P. C. Taylor, and L. Boisvert, 2021: Arctic cloud response to a perturbation in sea ice concentration: The North Water polynya. *J. Geophys. Res. Atmos.*, **126**, e2020JD034409, https://doi.org/10.1029/2020JD034409.

Morrison, A. L., J. E. Kay, H. Chepfer, R. Guzman, and V. Yettella, 2018: Isolating the liquid cloud response to recent Arctic sea ice variability using spaceborne lidar observations. *J. Geophys. Res. Atmos.*, **123**, 473–490, https://doi.org/10.1002/2017JD027248.

——, ——, W. R. Frey, H. Chepfer, and R. Guzman, 2019: Cloud response to Arctic sea ice loss and implications for future feedback in the CESM1 climate model. *J. Geophys. Res. Atmos.*, **124**, 1003–1020, https://doi.org/10.1029/2018JD029142.

Palm, S. P., S. T. Strey, J. Spinhirne, and T. Markus, 2010: Influence of Arctic sea ice extent on polar cloud fraction and vertical structure and implication for regional climate. *J. Geophys. Res.*, **115**, D21209, https://doi.org/10.1029/2010JD013900.

Philipp, D., M. Stengel, and B. Ahrens, 2020: Analyzing the Arctic feedback mechanism between sea ice and low-level clouds using 34 years of satellite observations. *J. Climate*, **33**, 7479–7501, https://doi.org/10.1175/JCLI-D-19-0895.1.

Royer, J. F., S. Planton, and M. Déqué, 1990: A sensitivity experiment for the removal of Arctic sea ice with the French spectral general circulation model. *Climate Dyn.*, **5** (1), 1–17, https://doi.org/10.1007/BF00195850.

Schweiger, A. J., R. W. Lindsay, S. Vavrus, and J. A. Francis, 2008: Relationships between Arctic sea ice and clouds during autumn. *J. Climate*, **21**, 4799–4810, https://doi.org/10.1175/2008JCLI2156.1.

Screen, J. A., and I. Simmonds, 2010a: The central role of diminishing sea ice in recent Arctic temperature amplification. *Nature*, **464**, 1334–1337, https://doi.org/10.1038/nature09051.

——, and ——, 2010b: Increasing fall-winter energy loss from the Arctic Ocean and its role in Arctic temperature amplification. *Geophys. Res. Lett.*, **37**, L16707, https://doi.org/10.1029/2010GL044136.

Serreze, M. C., and R. G. Barry, 2011: Processes and impacts of Arctic amplification: A research synthesis. *Global Planet. Change*, **77**, 85–96, https://doi.org/10.1016/j.gloplacha.2011.03.004.

Shupe, M. D., and J. M. Intrieri, 2004: Cloud radiative forcing of the Arctic surface: The influence of cloud properties, surface albedo, and solar zenith angle. *J. Climate*, **17**, 616–628, https://doi.org/10.1175/1520-0442(2004)017<0616:CRFOTA>2.0.CO;2.

Soden, B. J., A. J. Broccoli, and R. S. Hemmler, 2004: On the use of cloud forcing to estimate cloud feedback. *J. Climate*, **17**, 3661–3665, https://doi.org/10.1175/1520-0442(2004)017<3661:OTUOCF>2.0.CO;2.

Stroeve, J. C., T. Markus, L. Boisvert, J. Miller, and A. Barrett, 2014: Changes in Arctic melt season and implications for sea ice loss. *Geophys. Res. Lett.*, **41**, 1216–1225, https://doi.org/10.1002/2013GL058951.

Taylor, P. C., M. Cai, A. Hu, J. Meehl, W. Washington, and G. J. Zhang, 2013: A decomposition of feedback contributions to polar warming amplification. *J. Climate*, **26**, 7023–7043, https://doi.org/10.1175/JCLI-D-12-00696.1.

——, S. Kato, K.-M. Xu, and M. Cai, 2015: Covariance between Arctic sea ice and clouds within atmospheric state regimes at the satellite footprint level. *J. Geophys. Res. Atmos.*, **120**, 12 656–12 678, https://doi.org/10.1002/2015JD023520.

Tiedtke, M., 1993: Representation of clouds in large-scale models. *Mon. Wea. Rev.*, **121**, 3040–3061, https://doi.org/10.1175/1520-0493(1993)121<3040:ROCILS>2.0.CO;2.

Vavrus, S., 2004: The impact of cloud feedbacks on Arctic climate under greenhouse forcing. *J. Climate*, **17**, 603–615, https://doi.org/10.1175/1520-0442(2004)017<0603:TIOCFO>2.0.CO;2.

——, D. Waliser, A. Schweiger, and J. Francis, 2009: Simulations of 20th and 21st century Arctic cloud amount in the global climate models assessed in the IPCC AR4. *Climate Dyn.*, **33**, 1099–1115, https://doi.org/10.1007/s00382-008-0475-6.

——, M. M. Holland, and D. A. Bailey, 2011: Changes in Arctic clouds during intervals of rapid sea ice loss. *Climate Dyn.*, **36**, 1475–1489, https://doi.org/10.1007/s00382-010-0816-0.

Wetherald, R. T., and S. Manabe, 1988: Cloud feedback processes in a general circulation model. *J. Atmos. Sci.*, **45**, 1397–1416, https://doi.org/10.1175/1520-0469(1988)045<1397:CFPIAG>2.0.CO;2.

Wettstein, J. J., and C. Deser, 2014: Internal variability in projections of twenty-first century Arctic sea ice loss: Role of the large-scale atmospheric circulation. *J. Climate*, **27**, 527–550, https://doi.org/10.1175/JCLI-D-12-00839.1.

Wielicki, B. A., B. R. Barkstrom, E. F. Harrison, R. B. Lee III, G. L. Smith, and J. E. Cooper, 1996: Clouds and the Earth's Radiant Energy System (CERES): An Earth observing system experiment. *Bull. Amer. Meteor. Soc.*, **77**, 853–868, https://doi.org/10.1175/1520-0477(1996)077<0853:CATERE>2.0.CO;2.

Yeo, H., M.-H. Kim, S.-W. Son, J.-H. Jeong, J.-H. Yoon, B.-M. Kim, and S.-W. Kim, 2022: Arctic cloud properties and associated radiative effects in the three newer reanalysis datasets (ERA5, MERRA-2, JRA-55): Discrepancies and possible causes. *Atmos. Res.*, **270**, 106080, https://doi.org/10.1016/j.atmosres.2022.106080.

Zelinka, M. D., S. A. Klein, and D. L. Hartmann, 2012: Computing and partitioning cloud feedbacks using cloud property histograms. Part II: Attribution to changes in cloud amount, altitude, and optical depth. *J. Climate*, **25**, 3736–3754, https://doi.org/10.1175/JCLI-D-11-00249.1.

Zheng, Y., and Y. Ming, 2023: Low-level cloud budgets across sea-ice edges. *J. Climate*, **36**, 3–18, https://doi.org/10.1175/JCLI-D-22-0301.1.

Zygmuntowska, M., T. Mauritsen, J. Quaas, and L. Kaleschke, 2012: Arctic clouds and surface radiation—A critical comparison of satellite retrievals and the ERA-Interim reanalysis. *Atmos. Chem. Phys.*, **12**, 6667–6677, https://doi.org/10.5194/acp-12-6667-2012.